

CORINOS IV: Quantifying Baseline-Fitting Uncertainties in SO₂ Ice Measurements with JWST/MIRI

RACHEL E. GROSS ,¹ YAO-LUN YANG ,² L.ILSEDORE CLEEVES ,^{3,1} EWINE F. VAN DISHOECK ,^{4,5}
 ROBIN T. GARROD ,⁶ MIHWA JIN ,^{7,8} NAMI SAKAI ,² CHRISTOPHER N. SHINGLEDECKER ,⁹ JAEYEONG KIM ,¹⁰
 JENNIFER B. BERGNER ,¹¹ NEAL J. EVANS II ,¹² JOEL D. GREEN ,¹³ CHUL-HWAN KIM ,¹⁴ JEONG-EUN LEE ,¹⁴
 YUKI OKUDA ,^{15,16} WILL R.M. ROCHA ,¹⁷ BRIELLE SHOPE ,¹ AND HIMANSHU TYAGI ,¹⁸

¹University of Virginia, Department of Chemistry, Charlottesville, VA 22904, USA

²Star and Planet Formation Laboratory, RIKEN Pioneering Research Institute, Wako-shi, Saitama, 351-0198, Japan

³University of Virginia, Department of Astronomy, Charlottesville, VA 22904, USA

⁴Leiden Observatory, Leiden University, PO Box 9513, NL 2300 RA Leiden, The Netherlands

⁵Max Planck Institute for Extraterrestrial Physics, Garching, Germany

⁶Departments of Chemistry and Astronomy, University of Virginia, Charlottesville, VA 22904, USA

⁷Astrochemistry Laboratory, Code 691, NASA Goddard Space Flight Center, Greenbelt, MD 20771, USA

⁸Department of Physics, Catholic University of America, Washington, DC 20064, USA

⁹Department of Chemistry, Virginia Military Institute, Lexington, VA 24450, USA

¹⁰Korea Astronomy and Space Science Institute, 776 Daedeok-daero, Yuseong-gu, Daejeon 34055, Republic of Korea

¹¹Department of the Geophysical Sciences, University of Chicago, Chicago, IL 60637, USA

¹²Department of Astronomy, The University of Texas at Austin, Austin, TX 78712, USA

¹³Space Telescope Science Institute, Baltimore, 3700 San Martin Dr., MD 21218, USA

¹⁴Department of Physics and Astronomy, Seoul National University, 1 Gwanak-ro, Gwanak-gu, Seoul 08826, Korea

¹⁵NRC Herzberg Astronomy and Astrophysics, 5071 West Saanich Road, Victoria, BC, V9E 2E7, Canada

¹⁶Star and Planet Formation Laboratory, RIKEN Cluster for Pioneering Research, Wako-shi, Saitama, 351-0198, Japan

¹⁷Laboratory for Astrophysics, Leiden Observatory, Leiden University, PO Box 9513, NL 2300 RA Leiden, The Netherlands

¹⁸Department of Astronomy and Astrophysics, Tata Institute of Fundamental Research, Homi Bhabha Road, Colaba, Mumbai 400005, India

ABSTRACT

Sulfur dioxide (SO₂) ice has been tentatively detected in protostellar envelopes, but its reliability as a solid-state sulfur reservoir remains unclear. We present new measurements of SO₂ ice from 6.8-8.5 μ m toward four Class 0 protostars observed with JWST's Mid-Infrared (MIRI) Medium Resolution Spectrometer, as part of the COMs ORigin Investigated by the Next-generation Observatory in Space (CORINOS) program. The sample spans a luminosity range from 1 L_{\odot} (B335, IRAS 15398-3359) to 10 L_{\odot} (L483, Ser-emb 7). To assess continuum placement uncertainty in absorption spectra, we apply randomized polynomial fits over the restricted region. We fit laboratory spectra from the Leiden Ice Database for Astrochemistry (LIDA) using the open-source Python library `Omnifit`. We detect the 7.7 μ m CH₄ band in all sources and find its column density robust to baseline choice, providing a reference for evaluating the weaker SO₂ feature on its blue shoulder and quantifying baseline-related uncertainty. Three SO₂ laboratory ices were tested: pure SO₂ ice yields 0.3-1.2% of volatile sulfur may be locked in SO₂ ice (lower and upper limits); CH₃OH:SO₂ ice gives 0.02-0.18%, but with lower quality fitting. The best-fitting H₂O:SO₂ ice yields 0.2-0.9%, which we consider the most realistic. These ranges define plausible bounds on SO₂ ice abundances in our sample. We find evidence for SO₂ in Ser-emb 7, L483, and IRAS 15398-3359, but emphasize the noisy spectrum of B335 prevents a definitive detection. Comparing SO₂ ice abundances across the different environments, we assess how conditions influence role of SO₂ as a potential sulfur reservoir and implications for the longstanding “missing sulfur” problem.

Keywords: mid-infrared, JWST, spectroscopy, protostars

1. INTRODUCTION

Sulfur-bearing molecules are detected throughout the interstellar medium and across all stages of star formation, from dense clouds (e.g., [Navarro-Almaida et al. 2020](#); [Esplugues et al. 2022](#)) to protostars (e.g., [Blake et al. 1987](#); [Drozdovskaya et al. 2018](#)) to protoplanetary disks (e.g., [Fuente et al. 2010](#); [Semenov et al. 2018](#); [Laas & Caselli 2019](#)) and comets (e.g., [Smith et al. 1980](#); [Altweig et al. 2022](#)). Despite sulfur’s cosmic abundance ($S/H \sim 1.3 \times 10^{-5}$), observations in dense environments consistently recover only a small fraction of the expected sulfur budget ([Tieftrunk et al. 1994](#); [Wakelam et al. 2004](#); [Anderson et al. 2013](#); [McClure et al. 2023](#)). This long-standing depletion has motivated the idea that most sulfur resides in solid material on or within interstellar ices, yet its specific carriers remain uncertain. To date, OCS is the only sulfur-bearing species securely identified in the solid phase (e.g., [Palumbo et al. 1995](#); [Boogert et al. 2015](#); [McClure et al. 2023](#); [Boogert et al. 2022](#); [Santos et al. 2024](#); [Taillard et al. 2025](#)). A weak absorption feature near $7.6 \mu\text{m}$, first attributed to SO_2 in W33A and NGC 7538 IRS 1 ([Boogert et al. 1997](#)), has since been tentatively reported toward both molecular clouds ([McClure et al. 2023](#)) and protostars ([Rocha et al. 2024](#)), but the SO_2 band remains difficult to isolate because of blending with CH_4 , OCN^- , and complex organics. As a result, its underlying contribution is still uncertain, and further quantifying the SO_2 ice feature and its sensitivity to local protostellar condition will provide constraints for evolving astrochemical models to better predict how sulfur is distributed during planet formation.

Interpreting a weak feature like SO_2 can be challenging due to both overlap with other molecular ices and needing accurate estimates of the “ice-free” baseline (e.g., [Gibb et al. 2004](#); [Schutte et al. 1999](#); [Boogert et al. 2008](#)). On the first point, the SO_2 stretching mode near $7.6 \mu\text{m}$ is weak and blended with absorption from CH_4 , OCN^- , and complex organics, making it particularly sensitive to analysis (e.g., [Rocha et al. 2024](#)). On the second point, all ice absorption measurements require some estimate of the absorption-free continuum to accurately estimate ice optical depth and thus ice content. Protostellar ice features particularly in the mid-infrared are often broad and overlapping, making identification of relatively clean bandwidth challenging. As a result, small changes in baseline placement can significantly affect the shapes, depths, and integrated areas of absorption bands, leading to uncertainties in

derived abundances ([Boogert et al. 1997](#); [Rocha et al. 2024](#)). The spectral window between 6.8 – $8.6 \mu\text{m}$ is especially crowded, containing the CH_4 deformation mode at $7.7 \mu\text{m}$ ([Öberg et al. 2008](#)) along with deformation and bending modes of ethanol ($\text{CH}_3\text{CH}_2\text{OH}$), formate (HCOO^-), and acetaldehyde (CH_3CHO) at 7.24 and $7.43 \mu\text{m}$ ([Schutte et al. 1999](#); [Terwisscha van Scheltinga et al. 2018](#)). As a result, the SO_2 shoulder at $7.63 \mu\text{m}$ is susceptible to blending with multiple species, making robust identification difficult with previous facilities.

Despite these challenges, observational studies with earlier infrared telescopes, such as the Infrared Space Observatory (ISO; ([Gibb et al. 2004](#))) and Spitzer IRS ([Boogert et al. 2008, 2015](#)), have provided the data for much of our known ice inventory, including major mid-IR absorbers such as H_2O , CO , CO_2 , CH_4 , and NH_3 . Ground-based facilities like ESO’s Very Large Telescope (VLT), Subaru, Keck, and NASA’s Infrared Telescope Facility (IRTF), as well as AKARI, have further advanced our understanding of interstellar ices through targeted surveys, including large VLT programs of CO ice ([Pontoppidan et al. 2003](#)) and OCN^- ice ([van Broekhuizen et al. 2005](#)), along with broader efforts spanning multiple species ([Grim et al. 1991](#); [Dartois et al. 1999b,a](#); [Shimonishi et al. 2010](#); [Chu et al. 2020](#); [Perotti et al. 2021](#)). However, the sensitivity and resolving power of these facilities were insufficient to reliably isolate SO_2 from the CH_4 feature.

The improved sensitivity and spectral resolution of the James Webb Space Telescope (JWST) has revolutionized the study of ices. JWST programs have already begun to transform our knowledge of ices. The IceAge Early Release Science program (PID 1128) has provided initial ice compositions in dense molecular clouds before protostellar formation ([McClure et al. 2023](#)). The Guaranteed Time Observations Program JOYS (PID 1290; [Rocha et al. 2024](#); [Chen et al. 2024](#); [van Dishoeck et al. 2025](#)) targeted high and low-mass Class 0/I protostars. [Rocha et al. \(2024\)](#) applied laboratory data fitting with the ENIIGMA genetic-algorithm tool ([Rocha et al. 2021](#)), while [Chen et al. \(2024\)](#) analyzed the same JOYS data using a two-step spectral-fitting routine that combined least-squares and Markov chain Monte Carlo (MCMC) methods (e.g., [Foreman-Mackey et al. 2013](#)). These advances now allow weak and blended mid-infrared ice features to be measured with greater accuracy than was possible with previous facilities.

Complex organic molecules (COMs), which are carbon-bearing species containing at least six atoms, are

a link between simple ice species and the prebiotic building blocks that allow life as we know it to occur. COMs form efficiently via reactions of simple ices on dust grains, and then sublimate via numerous pathways to be detected in the gas (e.g., Herbst & van Dishoeck 2009; Jørgensen et al. 2016, 2020; van Dishoeck et al. 2021; van Dishoeck & Bergin 2021). COM detection in the solid phase, along with the simple species from which they form, has been challenging due to broad and overlapping vibrational modes in the infrared. Among COMs, methanol (CH_3OH) is the simplest COM that has been securely identified in interstellar ices across multiple vibrational bands (Grim et al. 1991; Dartois et al. 2003; Pontoppidan et al. 2004; Öberg et al. 2011a). Larger COMs such as ethanol ($\text{CH}_3\text{CH}_2\text{OH}$) and acetaldehyde (CH_3CHO) have been more difficult to identify due to their weaker absorption features and their overlap with stronger modes from abundant simple ices (Schutte et al. 1999; Yang et al. 2022; McClure et al. 2023). Despite extensive laboratory study identifying multiple features, observational detections have remained tentative and rely on single-feature absorption (e.g., Terwisscha van Scheltinga et al. 2018). In the context of this study, these COM bands are important primarily because they contribute to the blended absorption around $7.6\text{--}7.7\text{ }\mu\text{m}$ that complicates SO_2 identification.

In this study, we present a new method to evaluate the effect of baseline uncertainty on column density estimates, focusing on the SO_2 feature near $7.63\text{ }\mu\text{m}$. We apply this approach to JWST MIRI data from the CORINOS Cycle 1 General Observer program (Yang et al. 2022), which targets four isolated Class 0 protostars that span a range of luminosities and gas-phase COM activity. By conducting multiple baseline fits and modeling the resulting spectra with laboratory ice data, we assess the robustness of SO_2 detections and place constraints on its abundance relative to CH_4 . The paper is organized as follows: Section 2 introduces the target sources; Section 3 describes the data reduction process with further details in Yang et al. (2022); Section 4 outlines our baseline fitting and modeling approach; Section 5 presents the resulting fits and column density estimates; and Section 6 explores the implications for the missing sulfur problem and interpreting our results.

2. SOURCES

2.1. *IRAS 15398-3359*

IRAS 15398-3359 (B228) is a Class 0 protostar located in the Lupus I molecular cloud (e.g., Heyer & Graham 1989) at a distance of $154.9 \pm 3.4\text{ pc}$ (Galli et al. 2020). With a bolometric luminosity of $1.4\text{ }L_\odot$ and bolometric temperature of $T_{\text{bol}} = 50\text{ K}$ (Ohashi

et al. 2023), with an envelope mass of $1.2\text{ }M_\odot$ (Jørgensen et al. 2013). IRAS 15398-3359 serves as a key target for understanding early-stage low-mass star formation. Observations have detected molecular line emission in the outflows of this source (e.g., Okuda et al. 2021; Thieme et al. 2023). Simple ices like H_2O , CH_4 , and CH_3OH have also been detected with Spitzer in the envelope of this source (e.g., Öberg et al. 2008; Boogert et al. 2008). IRAS 15398-3359 has a rich inventory of warm carbon-chain molecules (CCMs), indicative of active warm carbon-chain chemistry (WCCC) (Sakai et al. 2009). This chemical behavior is consistent with models in which CH_4 ice formed in the prestellar phase is desorbed during protostellar heating, driving the formation of carbon-chain species (Aikawa et al. 2008; Sakai et al. 2008). Episodic accretion events may further contribute to this process by temporarily increasing the temperature in the envelope (Jørgensen et al. 2013), possibly enhancing thermal desorption of ice species.

2.2. *Ser-emb 7*

Ser-emb 7 is a Class 0 protostar located in the Serpens Main star-forming region at a distance of $\sim 436\text{ pc}$ (Ortiz-León et al. 2017). It has a relatively high bolometric luminosity of $7.9\text{ }L_\odot$ (Enoch et al. 2011), bolometric temperature of 58 K (Enoch et al. 2009) and calculated as a low-inclination system ~ 25 degrees. Ser-emb 7 has an envelope mass of $\sim 4.3\text{ }M_\odot$ (Enoch et al. 2011). This source exhibits evidence of compact continuum emission and outflow activity, though detailed constraints on the inner envelope and disk structure remain limited (Enoch et al. 2011). To date, there are no sulfur rich species in either gas or ice detected in this source (Bergner et al. 2019).

2.3. *L483*

L483 is a Class 0/I protostar located in the Aquila Rift at a distance of $\sim 200\text{ pc}$ (Ortiz-León et al. 2017; Jacobsen et al. 2019). It has a bolometric luminosity of $\sim 13\text{ }L_\odot$ and a bolometric temperature of $T_{\text{bol}} \sim 50\text{--}70\text{ K}$ (Jørgensen et al. 2002; Lee et al. 2015), with an envelope mass of $4.4\text{ }M_\odot$ (Jørgensen et al. 2004). L483 is embedded in a dense, asymmetric envelope and drives a prominent bipolar outflow seen in CO and H_2 line emission (Tafalla et al. 2000). It also exhibits strong ice absorption features and rich COM chemistry in both the gas (Jacobsen et al. 2019) and solid phase (Chu et al. 2020). Recent ALMA observations have revealed that L483 is in fact a *binary system* with a projected separation of $\sim 34\text{ au}$ (Cox et al. 2022; Hirota et al. 2025). No circumbinary disk larger than $\sim 30\text{ au}$ has been detected (Jacobsen et al. 2019; Cox et al. 2022), and

it remains unclear which component hosts the compact Keplerian disk previously inferred from continuum and C¹⁸O kinematics (Jacobsen et al. 2019). The system shows complex velocity structure, including SiO emission peaks located ~ 100 au northeast (blue-shifted) and ~ 200 au north (near systemic velocity) of the continuum peak, with their driving source still under debate (Hirota et al. 2025). Nevertheless, the overall north-blue / south-red velocity gradient traced by C¹⁸O, SO, and CS remains consistent with a moderately inclined rotating envelope. Observations with the IRAM 30m telescope found several sulfur-bearing species in the gas phase including CH₃SH, HCS, HSC, C₂S, H₂CS, and NS⁺, with CS being the most abundant (Agúndez et al. 2019). SO, OCS, and SO₂ were also detected at abundances comparable to those observed in cold pre-stellar cores such as TMC-1 (Agúndez et al. 2019).

2.4. B335

B335 is a nearby isolated Class 0 protostar at a distance of ~ 100 pc with a low bolometric luminosity of $\sim 1.5 L_{\odot}$ and is nearly edge-on with an inclination of ~ 87 degrees (Evans et al. 2015; Yen et al. 2015), and protostellar mass of $0.25 M_{\odot}$ and a disk mass of $0.063 M_{\odot}$ (Evans et al. 2023), with an envelope mass of $2.4 M_{\odot}$ (Saito et al. 1999). Its bolometric temperature is ~ 37 K (Okoda et al. 2024). B335 has been studied as a prototypical example of inside-out collapse and drives a slow, wide-angle bipolar outflow (Zhou et al. 1993; Harvey et al. 2001). B335 shows rich organic and deuterated chemistry (Imai et al. 2016; Okoda et al. 2022). It exhibits strong water and CO₂ ice absorption bands and faint features from methanol and ammonia (Boogert et al. 2008). Gas-phase SO₂ has been detected within 15 au of the protostar with ALMA (Bjerkeli et al. 2019). B335 is an important low-mass source for studying ice chemistry in isolated environments, and, as shown by Lee et al. (2025), its decade-long luminosity burst provides a unique opportunity to investigate how complex organic molecules and ices respond to protostellar variability.

3. OBSERVATIONS

All data presented in this paper were taken as part of program ID 2151 with the Mid-InfraRed Instrument (MIRI) (e.g., Rieke et al. 2015; Wright et al. 2015) in medium resolution mode (MRS) (e.g., Wells et al. 2015). For this program, all four integral field units (IFU) of the MIRI Medium Resolution Spectrometer (MRS) were used, covering 4.9 to 28 μ m. The observations allocated 1433.4 seconds to both the SHORT and LONG wavelength ranges, and 3631.3 seconds to the MEDIUM

range to allow higher signal/noise. The data were taken with the SLOWR1 standard read-out mode with four-point dither pattern (see also Yang et al. 2022, for further details). Some or all of the data presented in this article were obtained from the Mikulski Archive for Space Telescopes (MAST) at the Space Telescope Science Institute. The specific observations analyzed can be accessed via DOI: 10.17909/77j7-pd29. Data reduction was conducted using the JWST calibration pipeline version 1.15.1 (Bushouse et al. 2025), following methodologies outlined in Yang et al. (2022). The process included pixel-to-pixel background subtraction and fringe reduction steps in Stage 2. The outcome comprised 12 spectral cubes across the three wavelength ranges. Spectrum extraction was performed using photutils (Bradley et al. 2023), adopting a method that employs an aperture size four times the beam diameter, ranging from $0.38''$ to $2.17''$. For B335, which is significantly fainter and noisier, we used a fixed $1''$ aperture and additionally tested an extraction from a $1''$ offset position to reduce background contamination. The extracted spectra were then normalized by scaling flux densities from the shortest to the longest wavelengths to align median values across overlapping spectral segments. For B335 we did not apply subband scaling. The higher noise in each spectrum, which becomes worse toward the edges of each subband, makes the median-matching method unreliable and the scaling performs poorly. Without any scaling we do not see a substantial offset between subbands, suggesting that the original flux agreement is acceptable. The different appearance of the B335 spectrum is therefore mainly due to its higher noise level rather than intrinsic spectral structure. The resulting spectra typically reach rms noise levels of ~ 0.1 mJy in the 5–15 μ m region, increasing to ~ 0.15 – 0.2 mJy toward the longest wavelengths. These values are consistent with previous MIRI ice studies at similar integration times (e.g., Rocha et al. 2024).

4. METHODOLOGY

4.1. Baseline fitting

The first step in analyzing ice absorption spectra is to obtain an optical depth spectrum and isolate absorption features from the underlying background. Once the continuum is fit, then the optical depth is calculated using the standard relation:

$$\tau(\lambda) = -\ln \left(\frac{F(\lambda)}{C(\lambda)} \right) \quad (1)$$

where $F(\lambda)$ is the observed flux density and $C(\lambda)$ is the fitted continuum.

Figure 1 illustrates the challenge of identifying a “clean” baseline in ice rich sources. All four sources in-

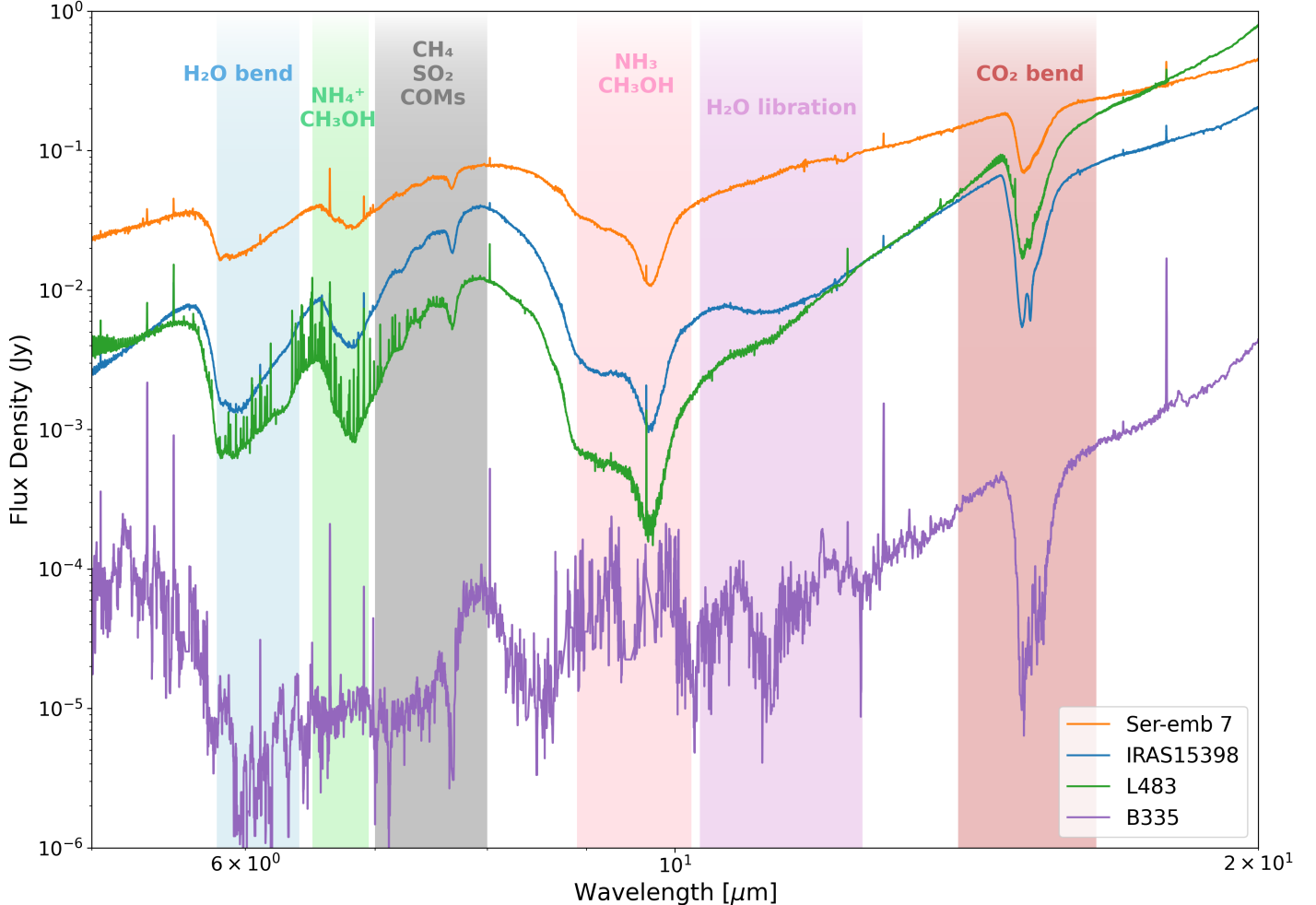


Figure 1. The flux density for all four sources in the CORINOS program. The grey highlighted region between 6.8–8.5 μm shows the blended COM region that this paper will focus. These are all 1D spectra extracted with a four-beam aperture with scaling for three of the sources (IRAS 15398-3359, Ser-emb 7, and L483). The sharp peaks in the spectra are from gas-phase species. Note the faintest source, B335, has no subband to subband scaling, and the spectrum is shown as extracted from individual MRS subbands.

crease in flux density with wavelength across the MIRI MRS range, consistent with embedded protostars. The strongly absorbed features observed in the spectra are attributed to various ice species including a broad water bending mode near 6 μm and silicate absorption near 10 μm . Between 7 and 8 μm lies the COM fingerprint region, which is the focus of our study, containing many species such as methane (CH_4), sulfur dioxide (SO_2), formic acid (HCOOH), ammonium (NH_4^+), acetic acid (CH_3COOH), and acetaldehyde (CH_3CHO), among others.

In ice rich regions like those described here, two approaches are taken, either a global approach that typically involves fitting a guided polynomial across the entire MIRI spectrum (e.g., Boogert et al. 2008; McClure et al. 2023; Rocha et al. 2025) or alternatively a local ap-

proach that breaks the spectrum into manageable ranges to better isolate the features of interest, particularly useful for blended features (Schutte et al. 1999; Rocha et al. 2024). Rayalacheruvu et al. (2025) introduced INDRA, a Python-based global fitting tool that performs continuum and silicate removal, then applies weighted non-negative least squares to fit the full MIRI spectrum, providing column densities and significance estimates while extending ice inventories to include organic refractories.

For the present study, we have opted to take a local approach since the features of interest SO_2 and CH_4 , are relatively weak and global fits can become dominated by fits to the strongest features. We specifically narrow our focus to the 6.8–8.5 μm spectral region and do not explicitly fit the silicate feature, as it primarily contributes to absorption beyond 9 μm . We first pre-

process the data by removing emission lines using a median filter (Huang et al. 1979) implemented with SciPy’s `median_filter` routine (Virtanen et al. 2020). In a median filter, the kernel size specifies the number of data points over which the median is computed. The filtering parameters were customized for each source: IRAS 15398 was smoothed using a 5-point kernel; for B335, NaN values were first removed, the sharp emission peaks masked and clipped followed by a median filter with a 5-point kernel; L483, which also contains prominent atomic and molecular emission lines, was first smoothed with a Savitzky-Golay filter (Savitzky & Golay 1964) as implemented in SciPy’s `savgol_filter` routine (Virtanen et al. 2020), then processed with a median filter with an 11-point kernel; and Ser-emb 7 was smoothed using a 5-point kernel.

Next, we fit a local baseline to isolate the absorption specific to the blended SO_2 and CH_4 feature. It is common in the literature to identify “by eye” a single, fixed polynomial continuum, making it difficult to assess how sensitive the derived column density is to this decision. To quantify the impact of choice of baseline, we introduce a statistical technique to estimate the baseline-attributed uncertainty. Within the 6.8–8.5 μm spectral range near the SO_2 feature, we identify smooth wavelength regions that are free of strong *local* ice absorption. We use these regions to estimate the variation in possible polynomial fits. For each estimate of the baseline, a single point is randomly selected within each of the spectral regions and used as a guide point to fit a third order polynomial. From preliminary testing, a third-order polynomial was determined to best fit the local continuum for all four sources. The wavelength regions identified for fitting SO_2 are marked as vertical grey bands in Figure 2, along with an example of the baseline fitting procedure and the resulting optical depth.

We followed the same procedure for each of our sources, except in the case of B335, which was substantially more noisy than the other sources. To keep the spectral guide points from falling into noise troughs when they were randomly selected, we took the median optical depth within each grey band for B335. We defined a $\pm 10\%$ window within that median value which allowed us to avoid noisy deviations. This also allowed us to avoid excessive smoothing that could alter the shape of the spectral features. We also note that in panel (d) of Figure 2, that the spectrum of B335 is very noisy red-ward of 8.2 μm . To avoid aggressive smoothing of the spectra past this wavelength we chose to limit the red side of our spectral fitting zone to 8.2 μm .

We repeat this randomized selection of polynomial anchor-points and fitting procedure fifty times for each source, producing a total of fifty optical depth spectra, referred to as “iterations” throughout this paper. The choice of fifty iterations reflects statistical completeness, providing sufficient sampling of baseline variability without oversampling redundant realizations. To visualize the effect of baseline variability, we selected two representative sources to show the outcome of the 50 randomized iterations (Figure 3): IRAS 15398–3359, which shows minimal variation across iterations, and B335, which exhibits substantially larger variation. These examples illustrate the extremes of baseline sensitivity in our dataset and provide a sense of the uncertainty range introduced by the fitting procedure.

This approach provides a statistical framework for assessing the uncertainties on the measured optical depth and thus column density introduced by baseline placement. Although some dependence on the adopted continuum windows and polynomial order remains, this method substantially reduces subjectivity compared to a single user-defined baseline.

4.2. Laboratory Data and *Omnifit*

To determine ice column densities from the MIRI spectra, we fit each observed optical depth spectrum with laboratory ice spectra from the Leiden Ice Database for Astrochemistry (LIDA) (Rocha et al. 2022). The chosen lab spectra (summarized in Table 1) cover the relevant 6.8–8.5 μm absorption features. The laboratory spectra include both pure and mixed ices designed to reproduce the molecular environments expected in interstellar and protostellar grain mantles. Mixed ices are prepared by combining two or more species under controlled conditions to examine how the surrounding matrix influences the shape and strength of absorption features. Each entry lists the constituents of the ice mixture and their corresponding ratios, the adopted band strength (A , cm molecule^{-1}) used to convert integrated optical depth to column density, and the temperature in Kelvin (K) at which the spectrum was measured in the laboratory.

The raw laboratory spectra are provided in absorbance units ($\text{Abs}_\nu = -\log 10(I/I_0)$), so we first convert them to optical depth using $\tau_\nu = \ln(10)\text{Abs}_\nu$ in order to directly compare with the observed τ_ν for each source. Each laboratory spectra is then interpolated onto the wavelength grid of the observations and smoothed to the JWST/MIRI spectral resolution. Because the lab data were measured with Fourier-transform infrared (FTIR) spectroscopy, some spurious interference fringes or baseline curvature can be present. We correct these by fitting a low-order polynomial, typ-

Table 1. Laboratory Ice Mixtures and Band Strengths used in Spectral Fitting

Structure	Formula	Name	Ice Mixture	λ (μm)	A (cm molec $^{-1}$)	Temp (K)	Ref.
	CH ₄	Methane	H ₂ O:CH ₃ OH:CO ₂ :CH ₄	7.67	9.6×10^{-18}	10	[1]
	CH ₃ CH ₂ OH	Ethanol	H ₂ O:CH ₃ CH ₂ OH (20:1)	7.01, 7.47	3.0×10^{-17}	15	[2]
	CH ₃ CHO	Acetaldehyde	H ₂ O:CH ₃ CHO (20:1)	7.23	1.4×10^{-17}	15	[2]
	SO ₂	Sulfur dioxide	pure, SO ₂ :CH ₃ OH (1:1) and SO ₂ :H ₂ O (1:10)	7.60	3.4×10^{-17} , 3.92×10^{-17}	10	[3,4]
	NH ₄ COOH	Ammonium formate	H ₂ O:NH ₄ COOH (7:100)	7.22, 7.41	1.0×10^{-17}	14	[5]
	CH ₃ COOH	Acetic acid	H ₂ O:CH ₃ COOH (10:1)	6.83, 6.89	1.9×10^{-17}	10	[6]
	HCOOCH ₃	Methyl formate	H ₂ O:HCOOCH ₃ (20:1)	7.75	2.52×10^{-17}	15	[7]
	H ₂ CO	Formaldehyde	pure H ₂ CO	7.75	1.4×10^{-17}	10	[8]
	OCN ⁻	Cyanate ion	pure OCN ⁻	7.6, 4.6	7.45×10^{-18} , 1.3×10^{-16}	12	[9,10]
	HCOOH	Formic acid	HCOOH:H ₂ O:CO (8:62:30), HCOOH:CO (11:89)	8.25, 4.67	2.9×10^{-17}	15	[2,6]
	CO	Carbon monoxide	CO:CH ₃ OH: CH ₃ CH ₂ OH (20:20:1)	4.67	1.4×10^{-17}	15	[2]

References. [1] Kerkhof et al. (1999); [2] Terwisscha van Scheltinga et al. (2018); [3] Boogert et al. (1997); [4] Yarnall & Hudson (2022); [5] Gálvez et al. (2010); [6] Bisschop et al. (2007); [7] Terwisscha van Scheltinga et al. (2021); [8] Gerakines et al. (1996); [9] Rocha et al. (2024); [10] van Broekhuizen et al. (2005).

Note: Data sourced from Leiden Ice Database for Astrochemistry (LIDA, Rocha et al. 2022), and the Cosmic Ice Laboratory database for reference [4]. The table shows the main species targeted in the 6.8 to 8.5 μm window, and whether each species was pure or mixed, along with ratios. Species that were used in fitting the OCN⁻ feature at 4.6 μm are also listed.

ically 2nd or 4th order, to the continuum baseline of the lab spectrum and subtracting it, producing a flattened baseline. This is an important step as any spurious features associated with the lab data could be misinterpreted when fitting to the observed spectrum. This results in a processed lab optical depth spectrum for each ice species that can be matched to the observational data.

Although our primary goal is to characterize the SO₂ and CH₄ ice features, we still must account for overlapping absorption from different ice components that have local features in the same wavelength range. In particular, we consider CH₃CH₂OH (ethanol), HCOOH (formic acid), NH₃:HCOOH mixtures which produce the anion HCOO⁻ upon acid-base reaction (e.g., Novozam-sky et al. 2001), OCN⁻ (cyanate ion), CH₃CHO (acetaldehyde), H₂CO (formaldehyde), HCOOCH₃ (methyl formate), and CH₃COOH (acetic acid) in addition to the target SO₂ and CH₄ (see Table 1 for a complete list).

This choice of additional ice components is based off preliminary trial and error with fitting laboratory data as well as guided by previous studies to fit this region showing that multiple components are likely to contribute to fitting the fingerprint region (Boogert et al. 1997; Yang et al. 2022; McClure et al. 2023; Rocha et al. 2024, 2025). Including these species in the model ensures that absorption near the SO₂ and CH₄ bands are properly fit by their likely carriers. Rocha et al. (2024) found that ten molecular ice components (including CH₄, SO₂, and the organics and ions listed above) are required to reproduce the MIRI spectra of protostars in this range, with CH₄ dominating the 7.7 μm band and species like OCN⁻, HCOO⁻, C₂H₅OH, and CH₃CHO contributing to the 7.2 and 7.4 μm features. Previous studies had also attributed the 7.24 and 7.41 μm ISO/Spitzer bands to combinations of HCOO⁻, C₂H₅OH, and CH₃CHO (Schutte et al. 1999; Öberg et al. 2011b). Guided by this prior work, our fitting includes the most relevant

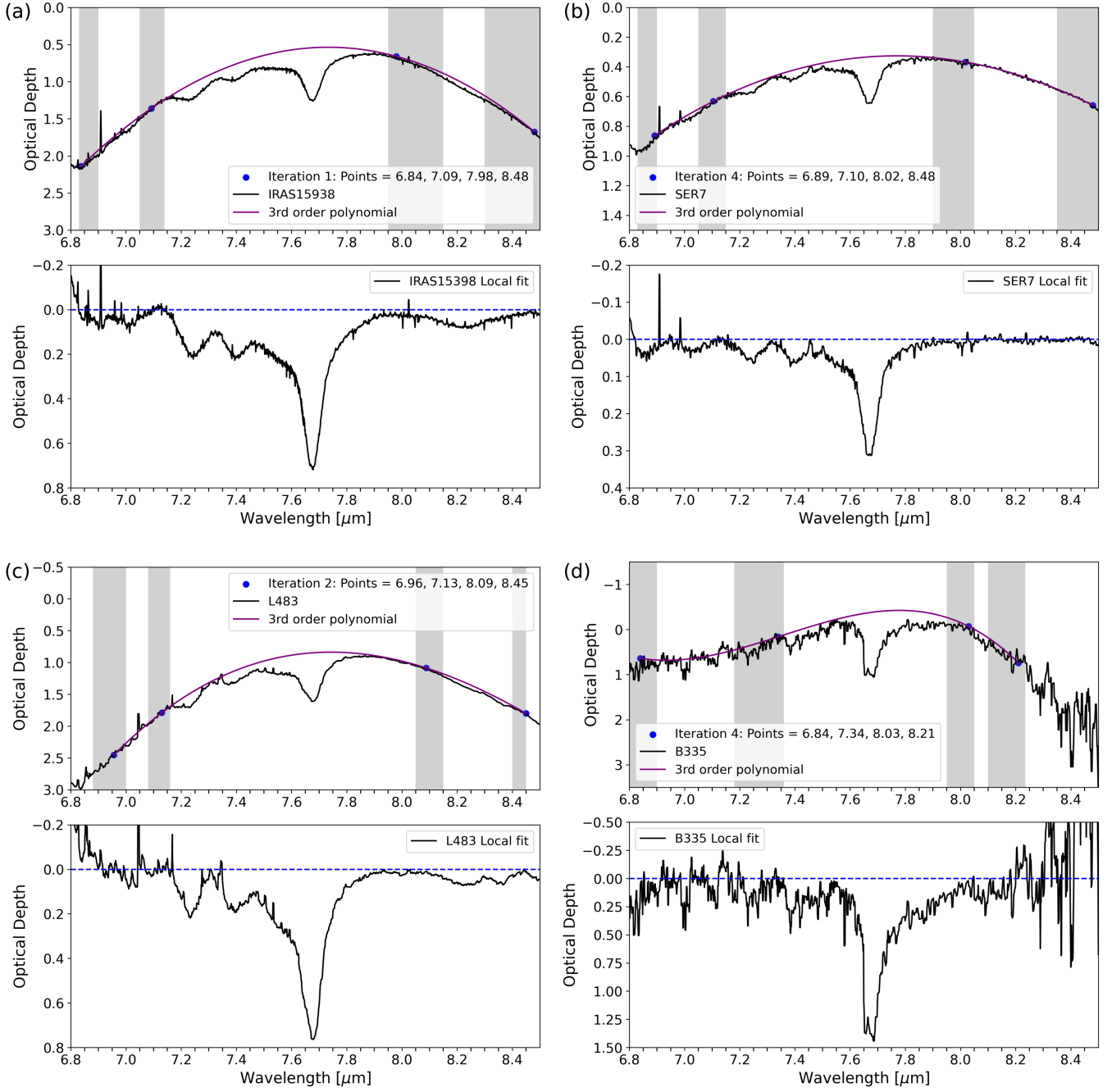


Figure 2. Example of baseline fits for each of the four CORINOS sources. The top plot with the vertical grey bars show the areas of minimal *local* ice absorption. This choice assumes that large absorption features (e.g., due to water or silicates) smoothly vary over our wavelength range that is fit by our polynomial. For each protostar one example set of guiding points is shown as blue markers, with the corresponding polynomial fit as a purple line. The resulting local optical depth spectra is shown below each panel. This process is repeated fifty times to generate different baseline subtracted optical depth spectra.

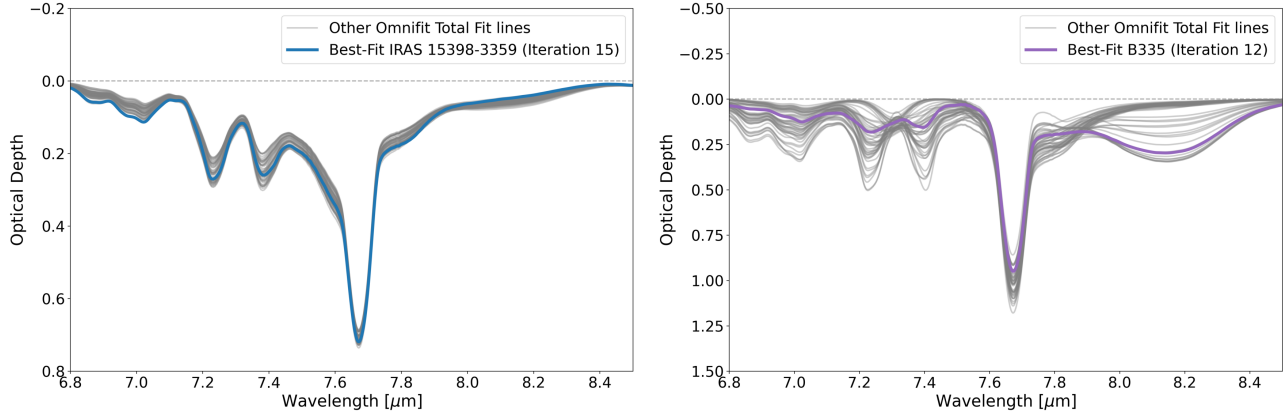


Figure 3. The colored line in each panel is the “best-fit” total `Omnifit` result out of the 50 baseline iterations using Reduced χ^2 for the pure SO₂ ice. The grey lines represent all other total fit lines. On the left panel, we show IRAS 15398-3359 as an example of a source with little variation in the fitting routine compared to B335 in the right side panel, whose fitting varies substantially with baseline choice.

ice candidates for the 6.8–8.5 μm region. We also examine how the fitted CH₄ column density varies under different baseline fits to provide context for the relative sensitivity of the SO₂ feature.

The spectral decomposition of the CORINOS sources using the laboratory data in Table 1 was carried out using `Omnifit`¹ and performs non-linear least-squares optimization via the `lmfit`² package to scale and fit multiple lab spectra to best match the observed absorption profile. The optimization routine developed by Suutari-nen (2015) is the Levenberg–Marquardt algorithm via `lmfit` that minimizes the following simplified expression:

$$\chi^2(\vec{a}) = \sum_{i=1}^N \left(\frac{y_i - f(x_i; \vec{a})}{\sigma_i} \right)^2 \quad (2)$$

y_i is the observed optical depth at wavelength i out of N data points, and $f(x_i; \vec{a})$ is the model’s predicted optical depth evaluated at the same wavelength x_i . The parameter \vec{a} are the scale factors that weight each laboratory spectrum. `Omnifit` starts with an initial input guess of scaling factor (0.0) and then finds the set of scalings until it minimizes $\chi^2(\vec{a})$.

The value σ_i is the per-point measurement uncertainty that is passed into the fitting routine, representing the random scatter remaining in each baseline-subtracted spectrum and serving as our estimate of the effective noise floor. To determine this quantity, we apply a 21-point kernel median filter to the optical-depth spectrum to produce a smooth continuum, then subtract it to ob-

tain the residuals. A 3- σ clipping is used to reject outliers, and the standard deviation of the remaining residuals defines σ_i . In `Omnifit`, this value is supplied as the constant error array so that each wavelength channel is weighted equally according to the measured noise level, σ_i . Figure 4 illustrates this procedure for IRAS 15398-3359 and B335, showing that the latter exhibits a noticeably higher noise level.

This standard deviation is used as a single, constant σ_i that `Omnifit` uses as the uncertainty at each wavelength (y_i). This allows the Levenberg–Marquardt algorithm to properly scale the contributions of each wavelength according to the actual noise level in the data. It will return both the best-fit amplitudes and their 1 σ_i errors from the covariance matrix. After fitting all the laboratory components `lmfit` reports the total χ^2 , as well as the reduced χ^2 which gives an average squared normalized residual per independent degree of freedom. The reduced χ^2 is used to determine the “best-fit” out of all the iterations for each source.

We verified that the features of SO₂ and CH₄ were being well reproduced once the nearby absorption features from species like formate and acetaldehyde were taken into account. In cases where a species was clearly not contributing, it was dropped from the final fit to reduce parameter degeneracy. The final `Omnifit` solution yields a scaled optical depth profile for each ice component, from which we can determine column densities. For each ice species, the column density N_{ice} molecules cm⁻² is derived from the fitted optical depth spectrum using the equation:

$$N_{\text{ice}} = \frac{1}{A} \int_{\nu_1}^{\nu_2} \tau_{\nu}^{\text{lab}} d\nu, \quad (3)$$

¹ `Omnifit` is an open-source Python library designed to interpret observational IR spectra.

² <https://lmfit.github.io/lmfit-py/>

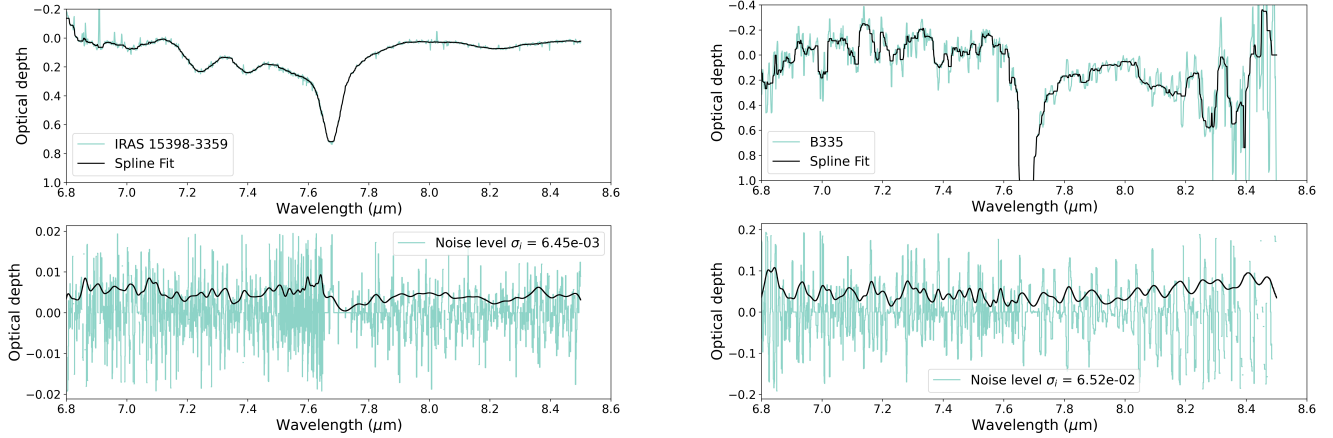


Figure 4. Example of fitting a spline to the local optical depth spectrum of IRAS 15398-3359, with the residuals used to derive the per-point noise level σ_i for `Omnifit`. Right: The same procedure is applied to B335, which yields a noticeably higher noise level.

where A is the band strength of the corresponding vibrational mode (in units of cm molecule^{-1}). The integral represents the integrated optical depth area of the absorption band from ν_1 to ν_2 , covering the frequency range on either side of the specific wavelength for each species in Table 1. A quantifies how much IR light a molecule absorbs at that wavelength and is measured in the laboratory by calibrating the absorbance with a known column density. The band strength A is not a universal constant for a given molecule, but can depend on the ice conditions such as temperature, phase, and mixture with other species (e.g., Öberg et al. 2007). Choosing lab spectra close to astrophysical ice conditions is important for obtaining accurate column densities.

The intensity of the band strength for the deformation mode of CH_4 at $7.7 \mu\text{m}$ increases when it is highly diluted in a mixture, but in a more 1:1 ratio the band strength is roughly 21-23 % stronger. H_2O is the most abundant ice in protostars, and is often the first to freeze onto dust grains due to its high sublimation temperature. H_2O therefore provides a matrix from which other species form, such as CH_4 (Qasim et al. 2018). Multiple compositions for testing mixtures of these species was used to best fit the $7.7 \mu\text{m}$ feature, and the best fit for our study was $\text{H}_2\text{O}:\text{CH}_3\text{OH}:\text{CO}_2:\text{CH}_4$ (0.4:0.6:1.0:0.23). The band strength for this mixture is $9.6 \times 10^{-18} \text{ cm molecule}^{-1}$ from Kerkhof et al. (1999). The SO_2 band strength is less sensitive to its environment, and so the same value can be used for the pure and $\text{CH}_3\text{OH}:\text{SO}_2$ ice. For the H_2O mixed SO_2 ice, we used a different band strength as water is the dominant component in the 10:1 laboratory ice and has a greater affect Yarnall & Hudson (2022). We have used the same care in selecting the band strength values for the other species in

our fits and the A values adopted in this work are listed in Table 1.

The mixture composition of the laboratory spectra not only affects the band strengths, but also the shapes and positions of the IR peaks. Species isolated in a pure ice can have different peak positions and intensities than when they are diluted in H_2O or CO_2 matrices (Ehrenfreund et al. 1997). We therefore used relevant laboratory mixtures when those are thought to better represent the interstellar ice matrix. Decades of laboratory work by various groups have produced an extensive archive of such spectra, including studies by Boogert et al. (1997); Gerakines et al. (1995); Öberg et al. (2007); Ehrenfreund et al. (1996), among others. Many of these are now accessible through databases such as LIDA (Rocha et al. 2022). Utilizing these resources and the guidance from recent JWST ice studies (e.g., McClure et al. 2023; Rocha et al. 2024), we were careful to include lab spectra that captures the most realistic combinations of mixtures for the ices in our sample.

The choice of laboratory ice spectra should also reflect the physical state of the observed ices. At low temperatures, ices are amorphous and display broad absorption features, while heating can induce crystallization, producing sharper and more structured IR bands (Dartois et al. 2015; Gudipati et al. 2023). The most widely used diagnostic of this process is the $3 \mu\text{m}$ H_2O stretching band in the near infrared or the $6 \mu\text{m}$ bending mode in the mid infrared, which shows clear structural changes with increasing temperature (Boogert et al. 2015). Additional heating diagnostics include the CO_2 bands: the $4.3 \mu\text{m}$ $^{13}\text{CO}_2$ stretching and $15.2 \mu\text{m}$ bending modes, both of which undergo characteristic profile changes as ices crystallize. Such features are especially clear in IRAS 15398-3359, as also noted by Yang et al. (2022).

Indeed, Kim et al. (in prep) find that fitting the global JWST MIRI spectrum of IRAS 15398–3359 requires at least two distinct H_2O ice temperature components to reproduce the observed profiles, suggesting a complex thermal history. This type of fitting also provides insight into the temperature evolution of the observed ices. By contrast, volatile organics such as CH_3OH , CH_3CHO , and SO_2 show only minor peak shifts or bandwidth changes at low temperatures (10–15 K). Significant profile changes emerge only once ices are warmed above ~ 70 K (Öberg et al. 2009; Rachid et al. 2020; Terwisscha van Scheltinga et al. 2021). For the 6.8–8.5 μm region analyzed here, we find that low-temperature (10–15 K) laboratory spectra provide the best match to the observed features in our CORINOS sample.

5. OMNIFIT RESULTS

5.1. CH_4 Ice Column Density

The prominent 7.7 μm absorption feature is clearly detected in all four protostellar spectra and is attributed to the ν_4 bending mode of CH_4 ice. This methane band is the main carrier in the 6.8–8.5 μm region (Öberg et al. 2008). IRAS 15398-3359 shows the CH_4 feature at an integrated $\tau_{\text{CH}_4} \sim 7 \text{ cm}^{-1}$ (peak $\tau \sim 0.5$), consistent with previous studies of low-mass protostars (Rocha et al. 2024). These values are higher than the previous fits of (Öberg et al. 2008), which found $\tau_{\text{CH}_4} \sim 4.2 \pm 0.8 \text{ cm}^{-1}$ using Spitzer IRS observations for this same source. The primary difference between the previous study and this one is that at the lower resolution ($R < 100$), the baseline could not account for “wiggles” that we now resolve as ice features with JWST in this wavelength range (see their Figure 1), and so the previous baseline had been too deep near CH_4 , reducing the calculated ice optical depth. L483 shows a similar integrated band area (integrated $\tau_{\text{CH}_4} \sim 7 \text{ cm}^{-1}$, peak $\tau_{\text{CH}_4} \sim 0.5$), while Seremb 7 is slightly weaker by roughly 20%. In contrast, B335 exhibits a much stronger CH_4 absorption (integrated τ_{CH_4} of 12 cm^{-1} and a peak $\tau_{\text{CH}_4} \sim 1$). From these fits, we derive CH_4 column densities on the order of $10^{17} - 10^{18} \text{ cm}^{-2}$ for the four sources (see Table 3). We note that the B335 spectrum approaches the noise floor across much of the 7–8 μm region. While we report derived column density values for completeness, they should be regarded as tentative measurements.

Across the different baseline fits, the derived CH_4 column densities remain relatively consistent, indicating that the feature is robust against moderate continuum variations. This stability provides an empirical reference for evaluating the greater baseline sensitivity of the weaker SO_2 absorption.

5.2. OCN^- Column Densities from NIRSpec

In order to more definitively determine the contribution of OCN^- to the 7.6 μm feature, it is necessary to use the 4.6 μm band in the near infrared. We use a simplified baseline fitting procedure here compared to our Monte Carlo approach applied to the MIRI data in this paper. The NIRSpec data for both B335 and IRAS 15398–3359 were used to estimate the column density for the 4.6 μm OCN^- band. The B335 data are from the JWST IPA program (ID: 1802; Federman et al. 2024), while the IRAS 15398-3359 data are from JWST program 1854 (PI: McClure). To our knowledge, no published NIRSpec observations of the 4.6 μm OCN^- band exist yet for L483 or Ser-emb 7. Without this near-IR constraint, the OCN^- column density cannot be reliably estimated from the 7.6 μm MIRI feature for those sources. As a result, a direct NIRSpec–MIRI comparison is only possible for B335 and IRAS 15398-3359, and we therefore restrict our OCN^- analysis in this section to these two objects.

To fit the baseline continuum for B335 we use a fourth order polynomial over ranges (4.0,4.2), (4.35,4.36), (4.51,4.52), (4.75,4.76), (4.8,4.85) to isolate the OCN^- feature. We smooth the spectrum gently with a median filter kernel=3. The resulting `Omnifit` fitting results are shown in Figure 5, and the column densities in Table 2. The 4.6 μm feature is blended with the CO stretching mode and therefore to properly fit this region, different mixtures of CO were tested.

We measure an OCN^- column density of $7.66 \times 10^{16} \text{ cm}^{-2}$ in the 4.6 μm feature. Our result is higher than the $5.0 \times 10^{16} \text{ cm}^{-2}$ reported for this same source in Nazari et al. (2024), but the two values are broadly consistent when the reported uncertainties and differences in continuum subtraction, spectral smoothing and fitting methods are taken into account.

Interestingly, our MIRI data does not reproduce the same strength OCN^- feature at 7.6 μm for the $\text{H}_2\text{O}:\text{SO}_2$ mixture, which had the best fit to the observed spectrum with only $6.30 \times 10^{15} \text{ cm}^{-2}$, one order of magnitude lower than the NIRSpec feature. Given multiple OCN^- detections in the NIRSpec 4.6 μm feature, we would expect a correspondingly stronger 7.6 μm band in the MIRI data; however, the poor quality of the B335 MIRI spectrum prevents a fair comparison in this source.

We followed the same procedure for IRAS 15398-3359’s NIRSpec data. We used a third order polynomial over ranges (4.35,4.36), (4.51,4.52), (4.75,4.76), (4.8,4.85) to draw our baseline continuum, and then subsequently fit with `Omnifit`. The spectrum is smoothed

Table 2. OCN[−] Column Densities and Adopted Band Strengths

Source	$\lambda_{\text{central}} (\mu\text{m})$	$N(\text{OCN}^-) (\text{cm}^{-2})$	$A (\text{cm molecule}^{-1})$	Reference
IRAS 15398–3359	4.62	1.20×10^{17}	1.30×10^{-16}	van Broekhuizen et al. (2005)
	7.62	3.58×10^{17}	7.45×10^{-18}	Rocha et al. (2024)
B335	4.62	7.66×10^{16}	1.30×10^{-16}	van Broekhuizen et al. (2005)
	7.62	6.30×10^{15}	7.45×10^{-18}	Rocha et al. (2024)

NOTE—The 7.62 μm column densities were measured using the H₂O:SO₂ (10:1) laboratory mixture of Yarnall & Hudson (2022).

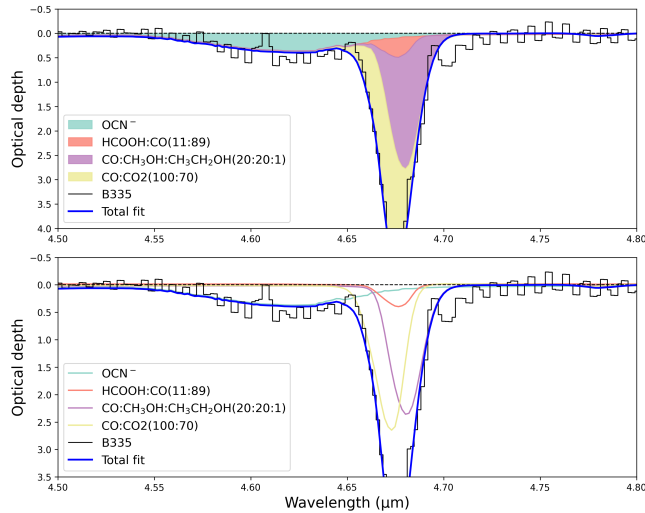


Figure 5. Fitting laboratory data to the 4.6 μm OCN[−] feature (teal) in NIRSpec data for source B335.

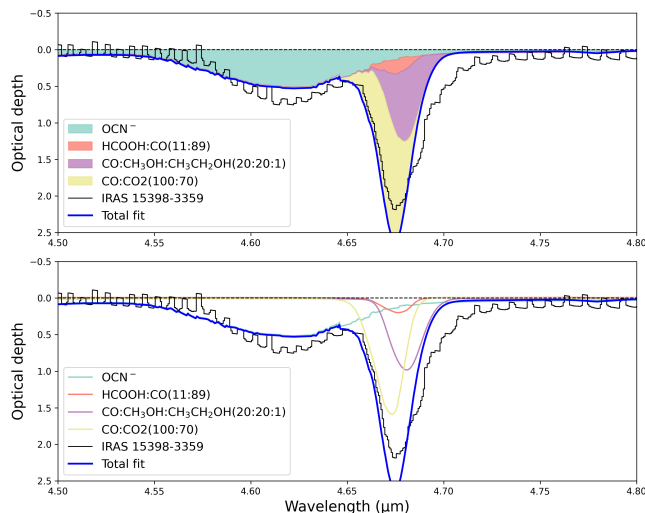


Figure 6. Fitting laboratory data to the 4.6 μm OCN[−] feature (teal) in NIRSpec data for source IRAS 15398-3359.

with a median filter kernel=7 to decrease the CO gas emission lines prominent in this region. The results are shown in Figure 6. The CO stretching feature is broader on the redward side at 4.67 μm , and therefore does not fit as well as this same feature for B335, indicating that we have not found quite the right CO mixture to best fit this source. However, the OCN[−] feature is fairly well reproduced, and comparing to the column density measurement from the H₂O:SO₂ mixture in the MIRI data showed values for both the 4.6 and 7.6 μm features similar, with $1.20 \times 10^{17} \text{ cm}^{-2}$ and $3.58 \times 10^{17} \text{ cm}^{-2}$, respectively. A more detailed discussion of the implications of these OCN[−] measurements, including their role in the blended 7.6 μm region and comparison with previous studies, is presented in Section 6.6. Importantly, our independent JWST NIRSpec detection of the 4.6 μm OCN[−] feature in IRAS 15398–3359 yielded a column density comparable to our derived value at the 7.6 μm feature when using the H₂O:SO₂ ice mixture, strengthening confidence in its presence in addition to SO₂.

5.3. SO₂ Column Density: Pure vs. Mixed Ices

On the blue-side of the CH₄ ice absorption there is a weak feature near 7.6 μm , which is attributed to the ν_3 asymmetric stretching vibrational mode of SO₂ ice. Identifying SO₂ in absorption has been challenging as it is weak and blended with nearby features, including those from complex organics like ethanol at 7.24 μm and formate near 7.25 μm (Boogert et al. 1997; Schutte et al. 1999). Boogert et al. (1997) found that the spectral shape, or profile, of the 7.6 μm feature of SO₂ is highly sensitive to its environment, and noted that laboratory data of pure SO₂ or SO₂ mixed with CH₃OH ices provided a good fit for high-mass protostellar sources W33A and NGC 7538. Rocha et al. (2024) found that the SO₂:CH₃OH mixture provided the best fit in their study as well for NGC 1333 IRAS2A and IRAS 23385+6053. While species are rarely in a pure matrix in interstellar ices, for completeness we fit the data using one pure SO₂ ice laboratory spectra and two spectra of SO₂ mixed

with CH_3OH ice (a $\text{SO}_2:\text{CH}_3\text{OH}$ mixture at 1:1 ratio) and mixed with H_2O (a $\text{H}_2\text{O}:\text{SO}_2$ mixture at 10:1 ratio; [Yarnall & Hudson 2022](#)). Given the complex ice spectra we see in these data, the SO_2 ice mixtures are considered to be more realistic fits for the SO_2 ice absorption. The laboratory data used to fit the feature at $7.6\text{ }\mu\text{m}$ are provided in Appendix A.

Pure SO_2 fit: Using the pure SO_2 laboratory spectra, significant SO_2 ice is necessary to reproduce the $7.6\text{ }\mu\text{m}$ shoulder in all four sources (red in Figure 7). The derived SO_2 column densities in these cases are of order 10^{17} cm^{-2} for IRAS 15398-3359 and L483, while the values for Ser-emb 7 and B335 are around 10^{16} cm^{-2} (Table 3). Ser-emb 7 has an average $N(\text{SO}_2) \sim 6.4 \times 10^{16}\text{ cm}^{-2}$ in the pure SO_2 fit, corresponding to an SO_2/CH_4 ratio of ~ 0.18 . L483 shows a similar ratio of $\text{SO}_2/\text{CH}_4 = 0.21$. IRAS 15398-3359 exhibits the highest ratio in the pure SO_2 case, about 0.27, with $N(\text{SO}_2) \sim 1.95 \times 10^{17}\text{ cm}^{-2}$. In contrast, B335's spectrum shows lower SO_2 column densities in the pure SO_2 ice scenario, where the $7.6\text{ }\mu\text{m}$ feature showing almost no blue shoulder, and yielding a lower ratio of ~ 0.04 and a column density of $\sim 5 \times 10^{16}\text{ cm}^{-2}$.

Gas-phase SO_2 has been reported toward B335, which suggests that an SO_2 ice reservoir should also be present (e.g., [Okoda et al. 2022](#)). However, our SO_2 ice detections in this source remain tentative given the current signal-to-noise level of the MIRI data, and the column density cannot be constrained with the same confidence as in the other three sources. While the best-fit values tentatively suggest a lower SO_2 ice abundance, this difference could reflect the higher noise in the B335 spectra rather than a true abundance variation. Optically thin isotopologue observations (e.g., $^{34}\text{SO}_2$), which would allow quantitative gas-phase column density estimates, have not yet been obtained for B335. Surveys of other protostars find SO_2 gas column densities typically in the range of $\sim 10^{16}\text{--}10^{17}\text{ cm}^{-2}$ ([Santos et al. 2024](#)), but without comparable measurements for this source, a direct gas-to-ice comparison is not possible. If future observations confirm that the SO_2 ice abundance is indeed lower than this typical gas-phase range, a plausible explanation could be partial sublimation of SO_2 -bearing ices during the recent luminosity burst reported by, which would enhance gas-phase SO_2 while potentially reducing its solid-phase abundance ([Lee et al. 2025](#)). In this scenario, the apparent low SO_2 ice abundance may reflect the effects of short-term heating from the recent luminosity burst rather than an intrinsic sulfur deficiency.

Mixed SO_2 with CH_3OH fit: Using the 1:1 mixed $\text{SO}_2:\text{CH}_3\text{OH}$ laboratory data, the contribution of SO_2 on the shoulder of the CH_4 ice absorption is lower for

all sources compared to the fit assuming pure SO_2 (Figure 8).

When the 1:1 $\text{SO}_2:\text{CH}_3\text{OH}$ mixture is used, the fitted SO_2 contribution decreases across all sources, while the OCN^- component becomes more prominent around $7.3\text{--}7.6\text{ }\mu\text{m}$. In these fits, the derived OCN^- column density increases by nearly an order of magnitude from about $\sim 1 \times 10^{17}\text{ cm}^{-2}$ in the pure or $\text{H}_2\text{O}:\text{SO}_2$ cases to about $\sim 1 \times 10^{18}\text{ cm}^{-2}$ with the $\text{SO}_2:\text{CH}_3\text{OH}$ mixture. This increase is unlikely to be physical because it exceeds the independently derived NIRSpec OCN^- column densities and occurs alongside a visibly poorer fit to the $7.4\text{--}7.6\text{ }\mu\text{m}$ shoulder (Figure 8). The most likely explanation is that this behavior arises from a fitting degeneracy in the modeling routine: because the weaker, broader $\text{SO}_2:\text{CH}_3\text{OH}$ band overlaps with the OCN^- profile, the algorithm can partially substitute one component for the other to minimize residuals. As a result, the fitting routine compensates for the reduced SO_2 contribution by increasing the OCN^- scaling to reproduce the local curvature. We therefore regard the resulting SO_2 column densities as lower limits to the SO_2/CH_4 ratio.

The CH_4 feature also appears slightly more blue-shifted than in the pure SO_2 case. In Ser-emb 7 and L483, the mixed-profile fits still find a non-zero SO_2 contribution, but lower by approximately an order of magnitude than in the pure case (Table 3). For instance, Ser-emb 7 and L483's SO_2/CH_4 ratio drops to ~ 0.04 with the mixed profile. In IRAS 15398-3359, the mixed-profile fit yields a very low SO_2 column of $N(\text{SO}_2) \sim 4 \times 10^{15}\text{ cm}^{-2}$, resulting in a ratio of $\text{SO}_2/\text{CH}_4 \sim 0.01$. B335's SO_2/CH_4 ratio is similarly small, with the SO_2 column density dropping by about a factor of three to $\sim 1.4 \times 10^{16}\text{ cm}^{-2}$. While the 1:1 $\text{SO}_2:\text{CH}_3\text{OH}$ mixture may still contribute to the CH_4 absorption profile, the pure and $\text{H}_2\text{O}:\text{SO}_2$ fits provide a better overall representation of the observed spectra.

Mixed SO_2 with H_2O fit: Using the $\text{H}_2\text{O}:\text{SO}_2$ (10:1) laboratory data, we find average SO_2/CH_4 ratios that fall in between the previous two cases. Ser-emb 7 and L483 have mean SO_2/CH_4 ratios of 0.12 and 0.15, respectively, while IRAS 15398-3359 has a slightly higher mean ratio at 0.2, comparable to the fit made using pure SO_2 (0.27). B335 has the lowest SO_2/CH_4 ratio of 0.05. Interestingly, we see a combination of the water-mixed SO_2 as well as OCN^- providing the optimal fit for the $7.6\text{ }\mu\text{m}$ feature for the three sources, IRAS 15398-3359, Ser-emb 7 and L483 (see Figure 9).

For these three sources, OCN^- contributes column densities of $\sim 1.8\text{--}7.9 \times 10^{17}\text{ cm}^{-2}$ for the $7.6\text{ }\mu\text{m}$ feature. These values are similar to those found in [Rocha et al. \(2024\)](#), where OCN^- was reported at a column density

Table 3. SO₂/CH₄ Ratios and Ice Column Densities

Source	Scenario	Mean N_{SO_2}	Mean N_{CH_4}	Mean ratio (SO ₂ /CH ₄) _{ice}	$N_{\text{H}_2\text{O}}(10^{19}\text{cm}^{-2})$
Ser-emb 7	Pure	0.64 ± 0.11	3.55 ± 0.08	0.18 ± 0.03	1.11
	CH ₃ OH:SO ₂	0.108 ± 0.077	2.82 ± 0.13	0.04 ± 0.03	...
	H ₂ O:SO ₂	0.382 ± 0.071	3.31 ± 0.08	0.12 ± 0.02	...
IRAS 15398-3359	Pure	1.95 ± 0.15	7.22 ± 0.09	0.27 ± 0.02	1.78
	CH ₃ OH:SO ₂	0.039 ± 0.11	5.26 ± 0.23	0.01 ± 0.03	...
	H ₂ O:SO ₂	1.32 ± 0.18	6.52 ± 0.14	0.20 ± 0.03	...
L483	Pure	1.79 ± 0.44	8.27 ± 0.35	0.21 ± 0.05	2.36
	CH ₃ OH:SO ₂	0.264 ± 0.23	6.64 ± 0.23	0.04 ± 0.04	...
	H ₂ O:SO ₂	1.07 ± 0.27	7.35 ± 0.16	0.15 ± 0.04	...
B335	Pure	0.58 ± 0.27	11.0 ± 1.02	0.05 ± 0.025	4.80
	CH ₃ OH:SO ₂	0.143 ± 0.63	21.6 ± 0.85	0.01 ± 0.02	...
	H ₂ O:SO ₂	0.566 ± 0.358	11.2 ± 1.082	0.05 ± 0.031	...

Notes. All column densities are in units of 10^{17} molecules cm^{-2} , unless noted. “Pure” denotes using a pure SO₂ laboratory spectrum; “CH₃OH:SO₂” denotes using a CH₃OH:SO₂ (1:1) lab mixture, and “H₂O:SO₂” denotes using a H₂O:SO₂ (10:1) lab mixture. Mean Ratio and column densities for SO₂ and CH₄ refers to the mean of all 50 baseline iterations. The error is derived from the standard deviation of the baseline uncertainty and the uncertainty in the `Omnifit` fitting, combined in quadrature for an absolute uncertainty. All values are derived from the optical depth fits in the 6.8–8.5 μm region. See Appendix 14 for fitting of H₂O ice column densities.

of $\sim 1 - 4 \times 10^{17} \text{cm}^{-2}$. The better overall fit to the data in this spectral range, the more realistic ice mixtures used, and the comparability to previous studies leads us to conclude that the fits using the H₂O:SO₂ (10:1) ice mixture is the most realistic of the three combinations of laboratory data we tested. The resulting SO₂/CH₄ ratios for this mixture are: Ser-emb 7: 0.12 ± 0.02, IRAS 15398-3359: 0.20 ± 0.03, L483: 0.15 ± 0.04, and B335: 0.05 ± 0.031. These three laboratory cases demonstrate the range of plausible SO₂ ice environments in our sample. Overall, despite source-to-source differences and baseline-driven uncertainties, the SO₂/CH₄ ratios are broadly consistent within a factor of two across the four protostars. Figure 10 shows the ratios from all three SO₂ laboratory ice cases (pure, CH₃OH:SO₂, H₂O:SO₂), and Table 3 lists the corresponding values.

5.4. Impact of Baseline Placement

The placement of the baseline is a significant factor contributing to systematic uncertainty in ice spectral fitting. This uncertainty is not from random spectral noise, but from the difficulty in determining the true underlying continuum beneath the absorption features. This is particularly relevant in observations characterized by low signal-to-noise ratios or in instances where the continuum is either partially or completely obscured by broad absorption features. Given that the continuum requires estimation rather than direct measurement, varying plausible baseline placements can result in different optical depth spectra, thereby affecting the results of spectral decomposition.

Each iteration in our study produces a slightly different continuum-subtracted optical depth spectrum. We utilize the reduced χ^2 value reported from `Omnifit`, that includes the consistent noise estimate outlined in the Methodology in Section 4.2. The resulting spread in reduced χ^2 values reflect how sensitive the total fit is to baseline choice. The value closest to unity is representative of the overall “best-fit” iteration.

Figure 3 demonstrates that IRAS 15398-3359 shows minimal variation between the best-fit and the other iterations, whereas B335 shows more substantial variation, reflecting the impact of lower signal-to-noise and weaker features on both baseline placement and the fitting routine. Notably, despite the larger spread in the total ice fits for B335, the standard deviation of the SO₂/CH₄ ratio remains relatively small, suggesting that SO₂ is intrinsically weaker than in the other targets, or we are approaching the noise floor for this source and therefore cannot confirm if SO₂ is present with our current data.

5.5. Absolute Uncertainty Estimation

To get an absolute error in our column density measurements, we combine in quadrature the two independent error terms: (1) the statistical uncertainty that `Omnifit`’s fitting routine determines from the scalings of the species (σ_{fit}), and (2) the systematic uncertainty induced by random baseline placement (σ_{base}), which is the standard deviation from our column density calculations for SO₂ and CH₄ for all fifty “iterations” from the `Omnifit` results. The contributions to the total uncer-

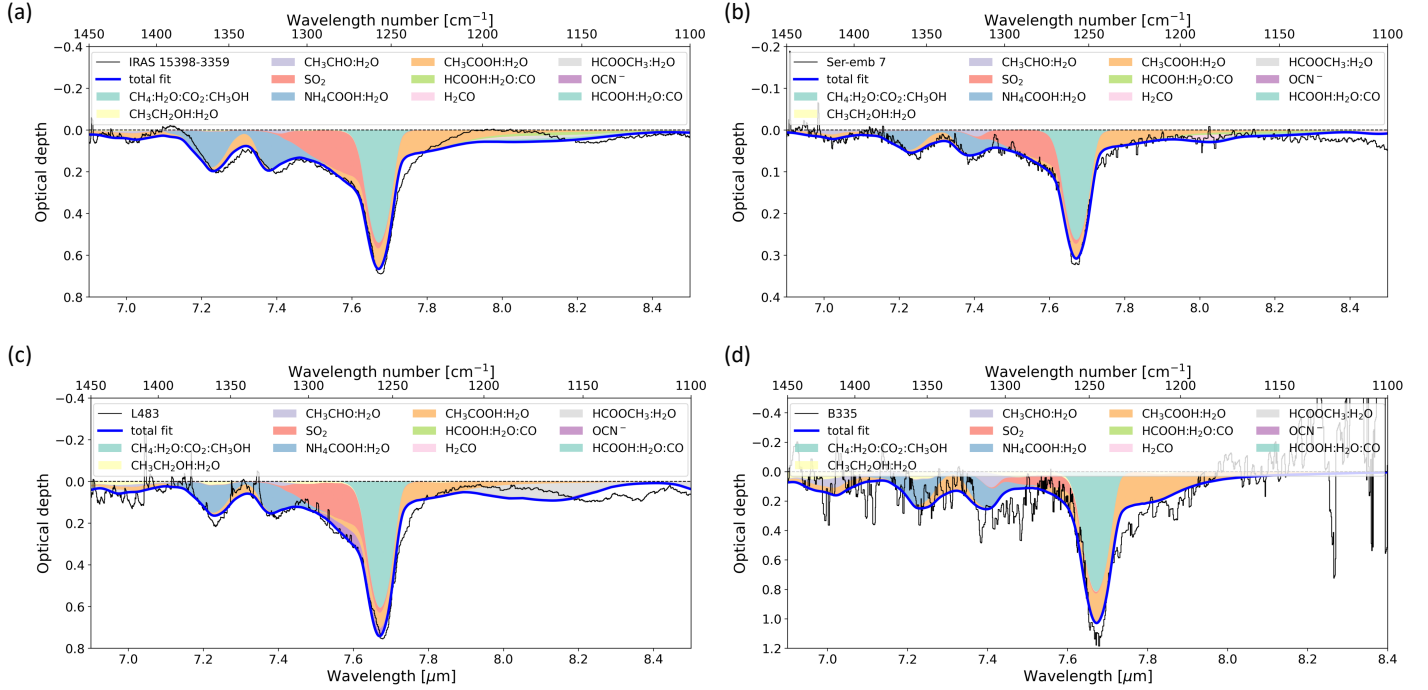


Figure 7. The Omnidfit results for a single iteration for each source with a pure SO_2 mixture.

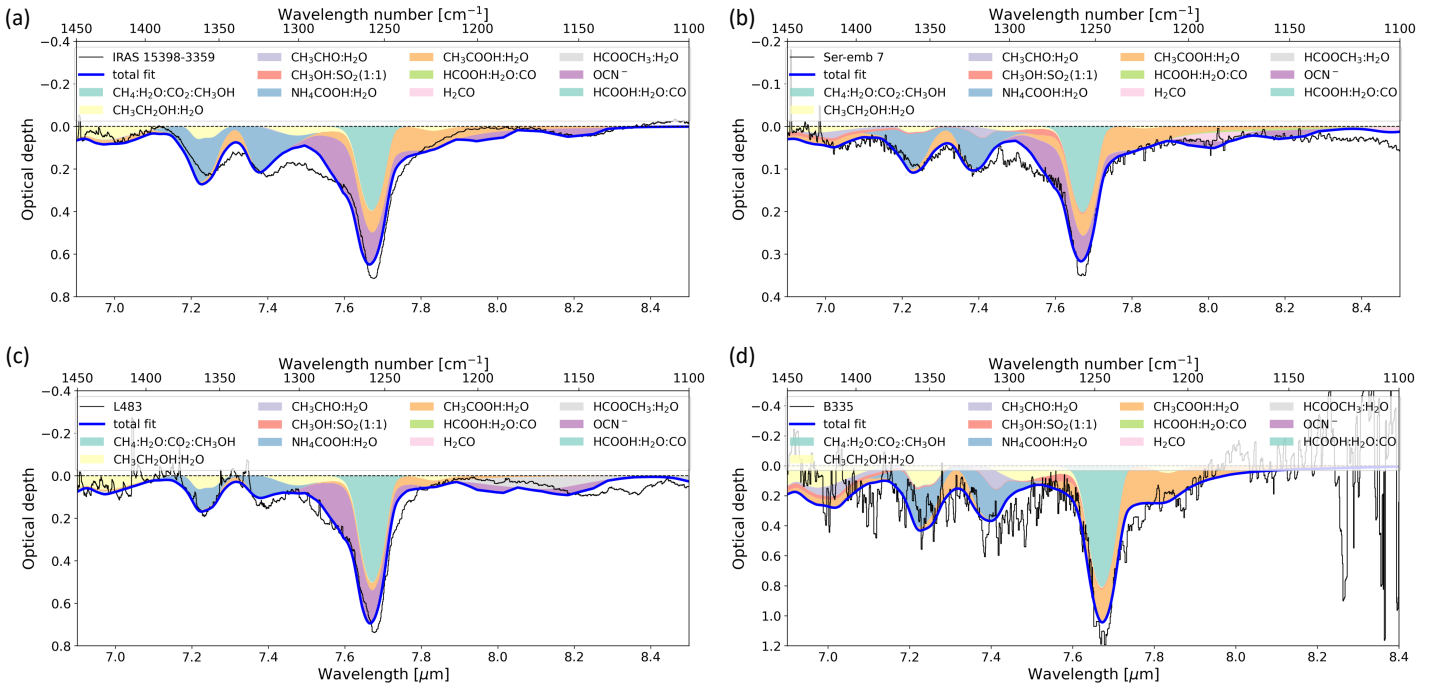


Figure 8. The Omnidfit results for a single iteration for each source with a $\text{SO}_2:\text{CH}_3\text{OH}$ mixture. All other laboratory data inputs remain the same as in the pure SO_2 case.

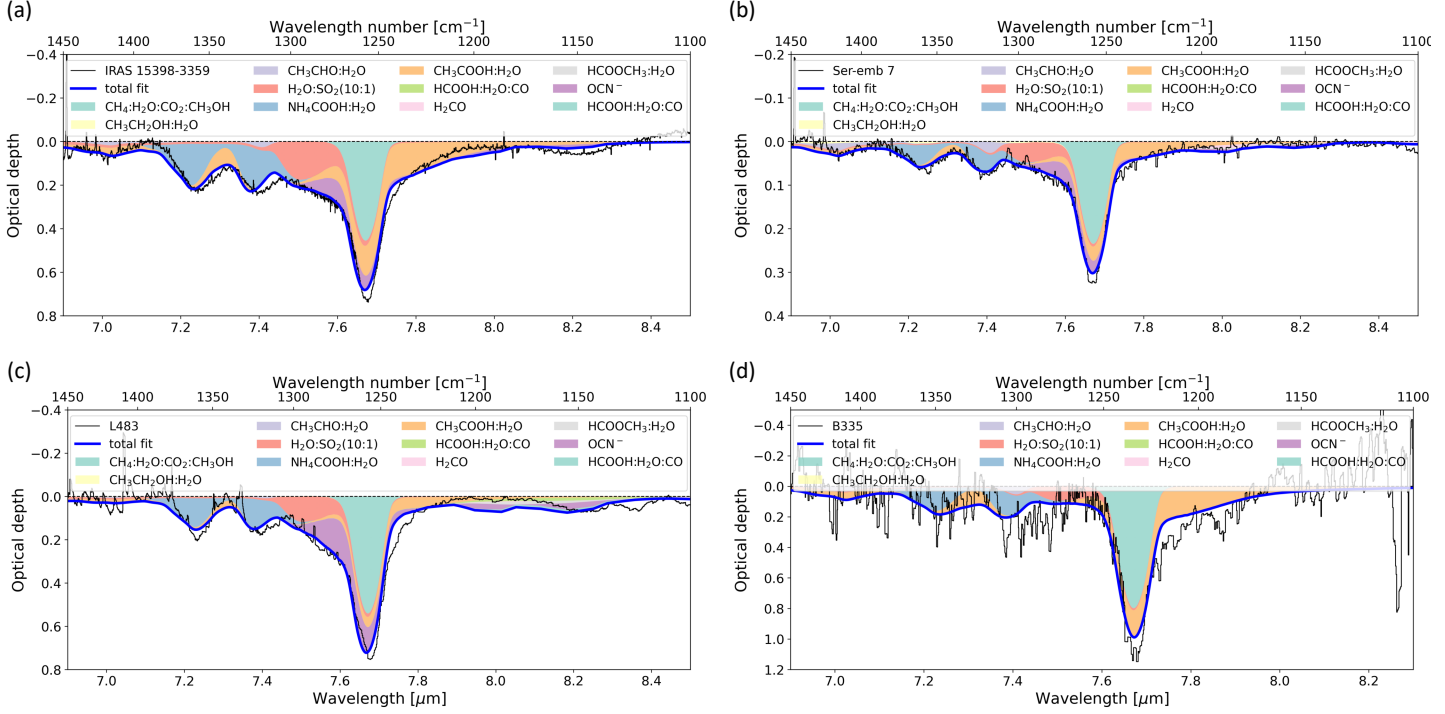


Figure 9. The `Omnidifit` results for a single iteration for each source with a $\text{H}_2\text{O}:\text{SO}_2$ (10:1) mixture. All other laboratory data inputs remain the same as in the pure SO_2 case.

tainty on the column density measurements from each of these sources is illustrated in Figure 11.

For example, the pure SO_2 scenario in the top row, the baseline uncertainty (blue) seems to dominate the column densities of SO_2 for all sources, but with the CH_4 column densities, the `Omnidifit` error (purple) contributes more to the overall uncertainty. For the fit using SO_2 mixed with CH_3OH the uncertainty contribution from `Omnidifit` and the choice baseline is closer to equal except for the case of B335. The latter is likely due to an increase in noise in the spectra and the resulting smoothing necessary before fitting. The $\text{H}_2\text{O}:\text{SO}_2$ mixture also showed more contribution from baseline uncertainty in the SO_2 column density measurements compared to the the CH_4 .

Collectively, we find that the choice of baseline dominates the uncertainty of derived column densities from weaker spectral features (SO_2) than than stronger ones (CH_4), as expected. However, in all cases, the choice of baseline introduces a non-negligible source of uncertainty in column density measurements compared to the uncertainty introduced by the multi-component ice fitting process alone.

6. DISCUSSION

6.1. Comparisons to Other Protostellar Regions

Rocha et al. (2024) reported SO_2 in the Class 0 sources IRAS2A and IRAS23385 using the same $\text{SO}_2/\text{CH}_3\text{OH}$ (1:1) ice mixture adopted in our analysis, with SO_2/CH_4 ratios of $\sim 0.04\text{--}0.12$, comparable to our results under the $\text{CH}_3\text{OH}:\text{SO}_2$ ice scenario. Similarly, the JWST IceAge program reported SO_2 in the Class I source Ced 110 IRS4A at $\sim 1.1 \times 10^{16} \text{ cm}^{-2}$, similar to our Ser-emb 7 result using the CH_3OH -mixed SO_2 ice (Rocha et al. 2025). However, in our spectra, the SO_2 mixed with H_2O laboratory data provided a much better fit to the $7.6 \mu\text{m}$ shoulder feature in Ser-emb 7, increasing the SO_2 column density to $\sim 3.8 \times 10^{16} \text{ cm}^{-2}$.

While not a direct comparison, the JWST IceAge program also tentatively detected SO_2 in dense molecular clouds, with $\text{SO}_2/\text{H}_2\text{O}$ upper limits of $\sim 0.1\text{--}0.3\%$, corresponding to column densities of $\sim 4 \times 10^{15} \text{ cm}^{-2}$. These are 1–2 orders of magnitude lower than our results, though their CH_4 column densities are comparable (McClure et al. 2023).

6.2. Availability of laboratory data

These results highlight the importance of ice matrix effects previously noted by Boogert et al. (1997), the profile of the $7.6 \mu\text{m}$ SO_2 band can vary with ice composition, which can affect how we decompose the blended spectral features in this region. A critical limitation in

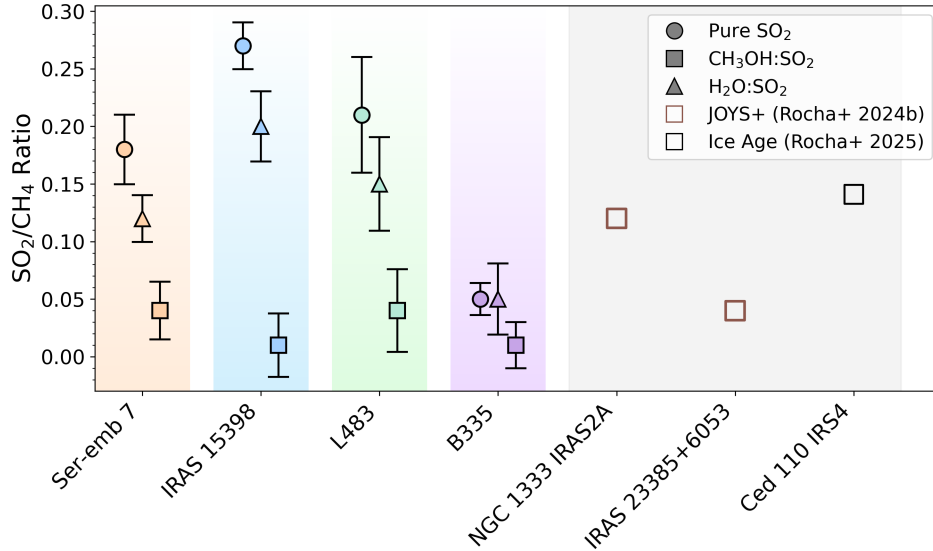


Figure 10. Average SO₂/CH₄ column density ratios for the four CORINOS sources. The different markers correspond to the different mixtures used to fit SO₂ described in Section 5.3. The error bars are the absolute uncertainty from both the baseline placement and the `Omnifit` uncertainty, described in Section 5.5. Despite minor source-to-source variations, the SO₂/CH₄ ratios are overall similar within a factor of two across the sample.

the interpretation for SO₂ ice for this type of study is the small amount of laboratory SO₂ mixtures available for download on the ice spectral databases. As also emphasized by Rocha et al. (2025), many spectral fits rely on just one or two SO₂ combination profiles, primarily SO₂:CH₃OH (1:1), which may not fully represent the diversity of the SO₂ ice environment. Expanded laboratory studies with SO₂ mixed with other major ice constituents across a range of temperatures and mixing ratios would significantly improve the fitting reliability and strengthen confidence in the detection and quantification of SO₂ ice.

6.3. Missing Sulfur

The depletion of sulfur in the gas phase by orders of magnitude relative to solar abundances has long been known as the “missing sulfur” problem (e.g., Woods et al. 2015; Laas & Caselli 2019). With a solar sulfur-to-hydrogen ratio of $[S/H]_{\odot} = 1.32 \times 10^{-5}$ (Asplund et al. 2009), only a small fraction, less than 1%, is observed in volatile forms in dense molecular clouds (McClure et al. 2023). While solid OCS is a securely identified sulfur-bearing ice (Boogert et al. 2022; McClure et al. 2023; Taillard et al. 2025), other sulfur ice species like SO₂ have been more challenging to detect due to their weak and often blended absorption features. Our new measurements of SO₂ ice in low-mass Class 0 sources provides increased evidence that a non-negligible portion of sulfur resides in the volatile ice reservoir.

For the three SO₂ scenarios considered in this paper, we estimate the amount of sulfur that could be locked

in SO₂ ice based on each fit (Table 4). We convert the SO₂/CH₄ ratios into SO₂/H by adopting CH₄/H₂O=1% (e.g., Gibb et al. 2004; Öberg et al. 2008; Boogert et al. 2015) and a water ice abundance H₂O/H = (2-6) $\times 10^{-5}$ consistent with dense cloud observations and protostellar envelopes (Boogert et al. 2015; van Dishoeck et al. 2021); we then express SO₂/H as a fraction of the solar sulfur abundance, $[S/H]_{\odot} = 1.32 \times 10^{-5}$ (Asplund et al. 2009). The exact conversion used is summarized in the notes to Table 4.

Adopting the H₂O:SO₂ (10:1) laboratory mixture as an illustrative “best-fit” example, the SO₂/CH₄ ratios translate to SO₂/H $\approx (0.24-1.20) \times 10^{-7}$, corresponding to roughly 0.2-0.9% of the solar sulfur budget. For the CH₃OH:SO₂ (1:1) mixture, the implied SO₂/H is lower at 0.02-0.18%, while the pure SO₂ case yields 0.3-1.2%. All ranges are summarized in Table 4.

These levels are also consistent with recent detectability estimates. Taillard et al. (2025) modeled JWST/MIRI thresholds for the 7.6 μ m SO₂ feature and found it should be identifiable at SO₂/H₂O ratios as low as $\sim 0.08\%$ for a 1 mJy continuum, rising to $\sim 0.5-1.0\%$ for fainter sources. Our inferred SO₂/H₂O $\sim 0.2\%$ lies within that accessible range for deep MIRI observations of embedded protostars.

Even with these detections, the S/H ratio from SO₂ ice remains $\sim 10^{-6}-10^{-7}$, still below the cosmic sulfur abundance, and indicating that the majority of sulfur resides in other reservoirs. Recent laboratory and modeling work investigates sulfur locked in more refractory

Table 4. Estimated $\text{SO}_2/\text{S}_\odot$ from this study

Laboratory Ice	$N_{\text{SO}_2}/N_{\text{CH}_4}$	$N_{\text{SO}_2}/N_{\text{H}} (10^{-7})^\dagger$	$\text{SO}_2/\text{S}_\odot (\%)^\dagger$
Pure SO_2	0.18–0.27	3.6–16.2	0.3–1.2
$\text{CH}_3\text{OH}:\text{SO}_2$ (1:1)	0.01–0.04	0.2–2.4	0.02–0.18
$\text{H}_2\text{O}:\text{SO}_2$ (10:1)	0.12–0.20	2.4–12.0	0.2–0.9

[†] $N_{\text{SO}_2}/N_{\text{H}}$ computed as $(N_{\text{SO}_2}/N_{\text{CH}_4}) \times (N_{\text{CH}_4}/N_{\text{H}_2\text{O}} = 0.01) \times (\text{H}_2\text{O}/\text{H})$, using $\text{H}_2\text{O}/\text{H} = 2 \times 10^{-5}$ (lower bound) to 6×10^{-5} (upper bound); then $\text{SO}_2/\text{S}_\odot = (N_{\text{SO}_2}/N_{\text{H}})/(1.32 \times 10^{-5}) \times 100\%$.

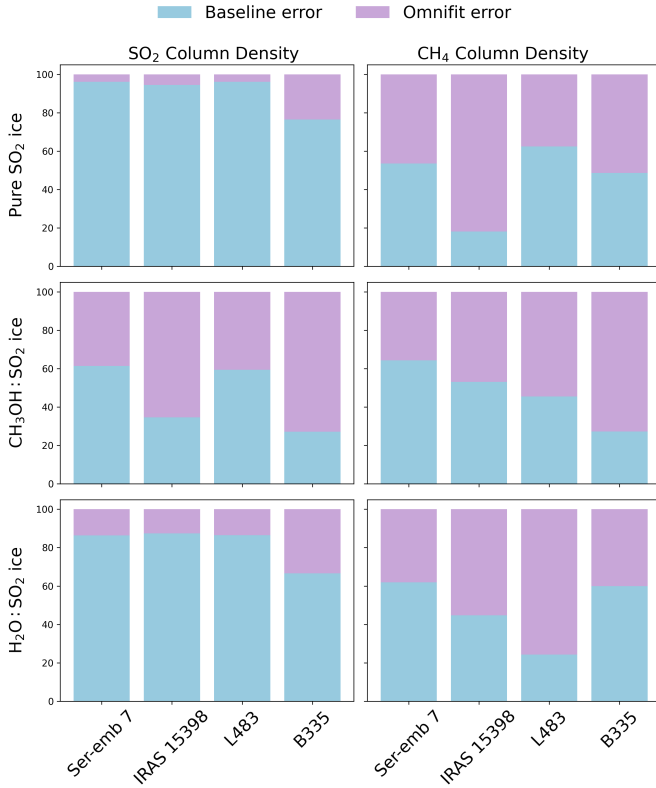


Figure 11. Contributions to the total uncertainty on the column density measurements from the placement of baselines (blue) and from **Omnifit**'s standard deviation from fitting the SO_2 and CH_4 (purple). Each row shows how the dominant uncertainty on the column density changes for CH_4 and SO_2 for each of the three cases discussed in the text: pure SO_2 , $\text{CH}_3\text{OH}:\text{SO}_2$, and $\text{H}_2\text{O}:\text{SO}_2$ laboratory data.

forms, including metal sulfides, sulfur allotropes like S_8 (Ferrari et al. 2024; Laas & Caselli 2019), or perhaps in ammonium hydrosulfide salts (Slavicinska et al. 2025). Slavicinska et al. (2025) demonstrated that the $6.85\ \mu\text{m}$ band which is attributed to NH_4^+ can be well fit by NH_4SH , or ammonium hydrosulfide. If most NH_4^+ is paired with SH^- , then NH_4SH could account for up to $\sim 18\%$ of the missing sulfur (Slavicinska et al. 2025). They also report the first tentative detection of SH^- via a weak $5.3\ \mu\text{m}$ feature, further supporting the role of ammonium salts as hidden sulfur reservoirs. These findings reinforce the idea that the missing sulfur is dis-

tributed among multiple reservoirs, and our new SO_2 measurements add to the inventory of volatile sulfur in the ice phase.

6.4. SO_2 Ice Formation and Chemical Origins

The detection of SO_2 ice in our sample of protostellar envelopes raises important questions about its chemical origins and formation history. Laboratory experiments demonstrate that UV and cosmic-ray irradiation of H_2S -rich ices rapidly destroys H_2S , efficiently producing oxidized sulfur species such as SO_2 and OCS , alongside refractory sulfur compounds (Garozzo et al. 2010; Chen et al. 2015). Similarly, UV photons generated by cosmic rays interacting with H_2 can photodissociate H_2O ice, producing abundant mobile OH radicals even at very low temperatures ($\sim 10\text{--}20\ \text{K}$; (Andersson et al. 2006; Andersson & van Dishoeck 2008; Ivlev et al. 2015; Shingledecker & Herbst 2018)), which can readily oxidize sulfur-bearing species such as S and SO into SO_2 (Hama & Watanabe 2013; Oba et al. 2018; Shingledecker et al. 2020). Hydrogen atom bombardment of H_2S ice also produces HS and S radicals that can be oxidized into SO_2 (Santos et al. 2024).

These pathways may operate across multiple evolutionary stages: during the prestellar phase, within collapsing envelopes, or even persisting into the earliest protostellar stages. Observations of gas-phase SO_2 and OCS in protostellar sources indicate that their abundances are consistent with an origin in early ice chemistry followed by desorption (Santos et al. 2024). At the same time, our observed SO_2 ice column densities ($\sim 10^{16} - 10^{17}\ \text{cm}^{-2}$) are consistent with ongoing production within cold protostellar envelopes. Taken together, these results suggest that the presence of SO_2 ice likely reflects contributions from both early and ongoing grain-surface chemistry, and does not indicate a major chemical reset. The low SO_2 abundances detected toward quiescent dense-cloud sightlines (e.g., McClure et al. 2023) further support this interpretation, demonstrating that SO_2 formation is inefficient under cold, weak-UV conditions and increases in response to the onset of protostellar processing.

Santos et al. (2024) emphasize that viable SO_2 formation pathways require a water-rich ice matrix, implying

that SO_2 ice formation likely occurs early, alongside H_2O ice and before significant CO freeze-out, when oxygen is abundant in water rather than locked in CO. Our observed SO_2 column densities ($\sim 10^{16} - 10^{17} \text{ cm}^{-2}$) suggest that a small yet significant fraction of sulfur remains trapped in these oxygen-rich ice forms. The presence of SO_2 ice may therefore serve as a valuable observational tracer of early-stage grain-surface oxygen chemistry, placing constraints on the timing and efficiency of sulfur incorporation into protostellar ice mantles.

These findings highlight the importance of studying Class 0 protostars, which represent the earliest evolutionary stage accessible for tracing volatile sulfur chemistry before it becomes more challenging to observe in later evolutionary phases. As protostars evolve toward Class II disk systems, increased UV irradiation, thermal desorption, and chemical reprocessing can obscure detections of simpler sulfur species such as SO_2 and SO. Nonetheless, strong detections of multiple SO_2 and SO transitions have been reported in certain disks, such as Oph IRS 48, and SO has been identified in additional disk surveys (Booth et al. 2021, 2024a,b). Surveys of embedded Class 0/I sources, such as PEACHES, frequently detect SO_2 gas, reinforcing its presence in cold, early protostellar environments and supporting the interpretation that sulfur-bearing ices like SO_2 predominantly form during the earliest stages of star formation (Artur de la Villarmois et al. 2023). For quantitative comparison with ice abundances, however, isotopologues such as $^{34}\text{SO}_2$ are required, since the main SO_2 lines can be optically thick (e.g., Booth et al. 2024b). For context, gas-phase $^{34}\text{SO}_2$ observations toward the Class 0 source IRAS 16293-2422 yield SO_2 column densities of order 10^{16} cm^{-2} (Drozdovskaya et al. 2018), about an order of magnitude lower than our solid-state SO_2 estimate for IRAS 15398-3359, suggesting that a substantial fraction of sulfur may remain in the ice at this stage.

While detailed analysis requires optically thin isotopologues, a tentative comparison of $\text{SO}_2/\text{CH}_3\text{OH}$ ratios in the gas and ice is still informative. In hot corinos and cores, gas-phase $\text{SO}_2/\text{CH}_3\text{OH}$ ratios are typically $\sim 10^{-4}$ – 10^{-3} (e.g., 1.3×10^{-4} in IRAS 16293B and 1.3×10^{-3} in G31.41; Belloche et al. (2025)). Using our SO_2/CH_4 average ratios of 0.1–0.2, combined with typical $\text{CH}_4/\text{CH}_3\text{OH}(\text{ice})$ values of 0.2–0.5 for Class 0/I protostars (Öberg et al. 2008; Boogert et al. 2015), corresponds to $\text{SO}_2/\text{CH}_3\text{OH}(\text{ice})$ ratios of ~ 0.02 – 0.10 . The relative ratio is $\sim 10^2$ – 10^3 times higher in the ice than in the hot gas, indicating that the observed SO_2 can be fully supplied by release from ices (e.g., sublimation or sputtering), and that its lower gas-phase abundance

likely reflects chemical processing during and after release.

6.5. Evaluating Environmental Factors on the SO_2/CH_4 Ratio

One goal of the CORINOS program is to determine which environmental factors regulate ice-phase sulfur abundances in Class 0 protostars. We examine the roles of protostellar luminosity, envelope mass, water-ice column density, and source inclination using our four CORINOS targets together with the additional protostars discussed in Section 6.1 (Ced 110 IRS4A/B, IRAS 2A, and IRAS 23385+6053). Although the combined sample remains small, a comparison allows us to evaluate whether any broad trends emerge in the SO_2/CH_4 ratio.

Protostellar luminosity is often invoked as a driver of ice processing, with the strongest effects expected for highly volatile species such as CO (Boogert et al. 2008; Öberg et al. 2011b). CH_4 is less sensitive to heating because it is frequently trapped in H_2O -rich matrices, while the temperature-dependent behavior of SO_2 in ices is less well constrained. Figure 12a shows how SO_2/CH_4 varies with bolometric luminosity (L_{bol}) across both the CORINOS and comparison sources. No systematic trend is seen. B335 and IRAS 15398–3359, the two least luminous objects, lie at opposite extremes of the observed ratio range, while the more luminous Ser-emb 7 and L483 cluster at intermediate values. B335 is a known outlier due to its prior luminosity burst (Lee et al. 2025), and its SO_2 absorption measurement is highly uncertain because of spectral noise. These comparisons indicate that luminosity alone does not control the SO_2/CH_4 ratio, consistent with Santos et al. (2024), who reported no link between luminosity and $\text{SO}_2/\text{CH}_3\text{OH}$ abundance ratios. Our measurements therefore contribute several new jointly measured SO_2 and CH_4 ice abundances to the literature, although the sample is still too small to identify luminosity-dependent behavior.

We next examine whether water-ice column density correlates with the SO_2/CH_4 ratio (Figure 12b). Across both the CORINOS and comparison protostars, no clear trend is present. B335, which has the highest H_2O column in our sample, shows one of the lowest SO_2/CH_4 ratios, though this value is highly uncertain due to spectral noise. Ser-emb 7 has the lowest water column among the CORINOS targets yet exhibits an intermediate SO_2/CH_4 ratio. The comparison protostars show similar scatter: IRAS 2A and Ced 110 IRS4A/B span a modest range of H_2O columns while occupying overlapping SO_2/CH_4 values, and IRAS 23385+6053 lies at the low end of both H_2O column and SO_2/CH_4 . Dense cloud

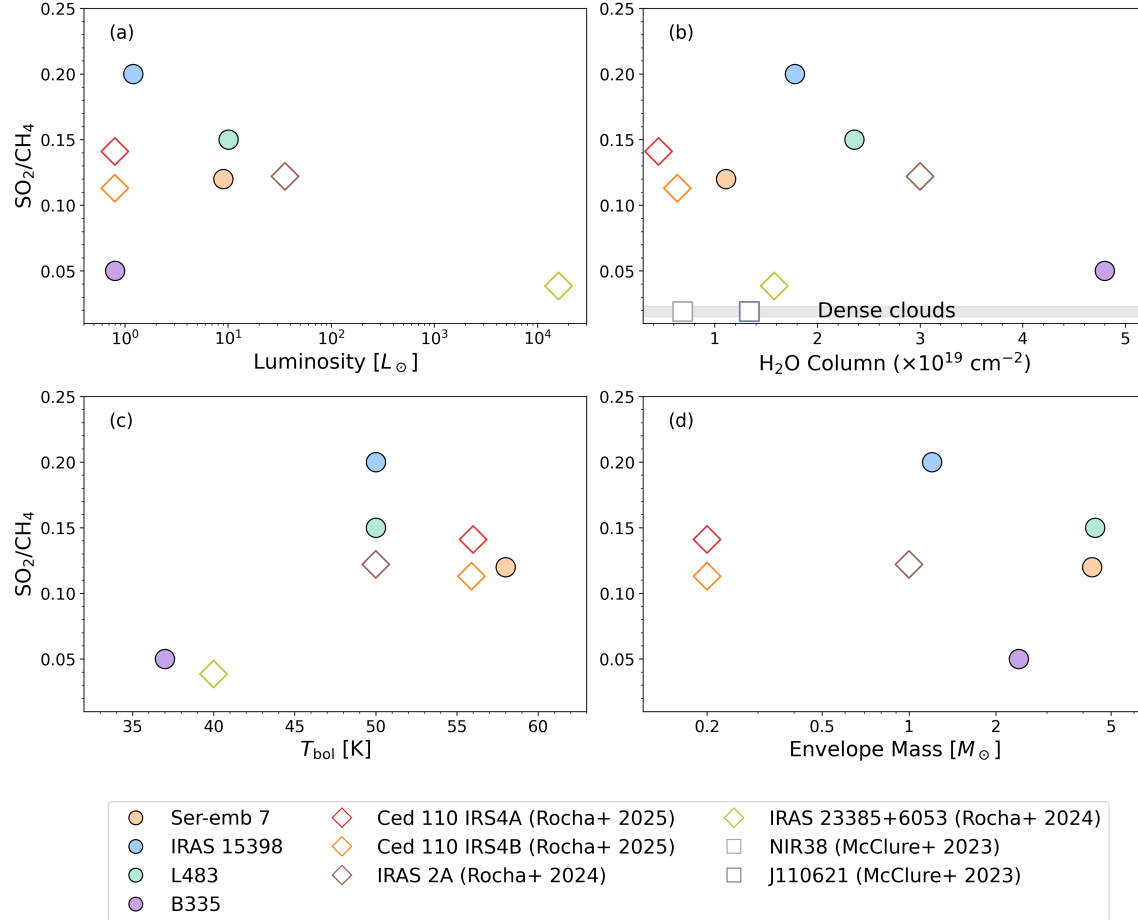


Figure 12. (a) SO_2/CH_4 ratio versus bolometric luminosity for the CORINOS sources and the comparison protostars discussed in Section 6.1 (Ced 110 IRS4A/B, IRAS 2A, and IRAS 23385+6053). (b) SO_2/CH_4 ratio versus H_2O ice column density. Dense cloud sightlines from the IceAge program (McClure et al. 2023, NIR38 and J110621) are shown as gray squares, and the shaded region marks the SO_2/CH_4 range observed in molecular cloud ices. (c) SO_2/CH_4 ratio versus bolometric temperature (T_{bol}) for both the CORINOS targets and the comparison protostars. T_{bol} for IRAS 2A and Ced 110 IRS4A/B are taken from Lee et al. (2015); the value for IRAS 23385+6053 is from Francis et al. (2024). (d) SO_2/CH_4 ratio versus envelope mass. Envelope masses for Ced 110 IRS4A/B are taken from San José-García et al. (2013), and the envelope mass for IRAS 2A is taken from Jørgensen et al. (2004). IRAS 23385+6053 is excluded from this panel because its envelope mass is not reliably constrained. The CORINOS values use the mean SO_2/CH_4 ratios from Table 5, derived from the $\text{H}_2\text{O}:\text{SO}_2$ laboratory fits.

sightlines (NIR38 and J110621) appear in the shaded region at the bottom of the panel, where SO_2/CH_4 values are an order of magnitude lower than in protostars despite comparable or higher water columns. These comparisons show that total H_2O ice column density does not set the SO_2 abundance. Instead, SO_2 production likely depends on the availability of chemical precursors such as atomic S and OH and on early prestellar ice chemistry rather than on the bulk amount of water ice (Santos et al. 2024; Rocha et al. 2025).

T_{bol} is a standard indicator of protostellar evolutionary stage, defined as the temperature of a blackbody with the same mean frequency as the observed SED (Myers & Ladd 1993). Values below roughly 70 K correspond to the deeply embedded Class 0 phase (Chen et al.

1995). When we compare SO_2/CH_4 with T_{bol} for the CORINOS and comparison sources (Figure 12c), the ratios remain clustered across the Class 0 range (35–70 K). The coldest objects, including IRAS 23385+6053 and B335, show the lowest ratios, while the slightly warmer Class 0 protostars occupy intermediate values. Although the sample is limited, this pattern suggests that the very earliest, coldest stages may be relatively SO_2 -poor compared to CH_4 .

We also examined whether the SO_2/CH_4 ratio correlates with envelope mass (Figure 12d). Across the CORINOS sources and the comparison protostars introduced in Section 6.1, the ratios occupy a similar range over more than an order of magnitude in envelope mass. The lowest SO_2/CH_4 values occur toward

IRAS 23385+6053 ($M_{\text{env}} \approx 0.2 M_{\odot}$; [Rocha et al. 2024](#)) and B335 ($M_{\text{env}} \approx 2.4 M_{\odot}$; this work) despite their very different envelope masses. Ser-emb 7 and L483, which host the most massive envelopes in the sample ($4\text{--}5 M_{\odot}$; [Jørgensen et al. 2004](#)), show intermediate ratios similar to lower-mass systems. Ced 110 IRS4A and IRS4B, which also host low-mass envelopes ($\sim 0.2 M_{\odot}$; [San José-García et al. 2013](#)), fall within the same overall distribution. This pattern indicates that bulk envelope mass is not the dominant factor controlling SO_2 ice abundance and instead points toward chemical conditions inherited from prestellar or very early protostellar stages.

Lastly, we explored whether source inclination influences the SO_2/CH_4 ratio. Our sample spans a broad range of viewing geometries, from nearly face-on (Ser-emb 7, $i \sim 25^{\circ}$) to moderately inclined (L483 and IRAS 15398–3359, $i \sim 70^{\circ}$). L483 is a confirmed binary system ([Cox et al. 2022](#)), and although its envelope shows a moderately inclined rotation pattern ([Jacobsen et al. 2019; Hirota et al. 2025](#)), the inclinations of the individual circumstellar disks are unknown. This unresolved structure introduces additional uncertainty when interpreting inclination-dependent behavior. More edge-on sightlines are expected to probe denser envelope and midplane material, enhancing ice absorption ([Pontoppidan et al. 2005; Crapsi et al. 2008; Tobin et al. 2008](#)). JWST studies likewise indicate that moderately inclined sightlines may underestimate ice columns by missing the regions where most ices reside ([Rocha et al. 2025](#)), and radiative transfer models show that CO , CO_2 , and H_2O absorption often originates at radii of order ~ 1000 au ([Thompson et al., in prep.](#)). However, within our sample, the SO_2/CH_4 ratio does not vary systematically with inclination. Geometry therefore influences total ice column but does not appear to regulate relative SO_2 abundances.

Overall, no clear correlations are found between SO_2/CH_4 and protostellar luminosity, envelope mass, water column density, or inclination. The ratios are broadly similar across diverse physical environments, suggesting that macroscopic source properties do not strongly regulate SO_2 ice abundance. A more likely explanation is that the observed ratios reflect underlying chemical conditions such as the prestellar sulfur reservoir, grain-surface chemistry prior to collapse, or variations in cosmic-ray ionization rate rather than later-stage protostellar evolution or geometry ([Vastel et al. 2018; Bulut et al. 2021](#)). This interpretation is supported by recent JWST observations of Ced 110 IRS4, which show that ice-phase chemistry changes little after initial formation in the pre-collapse stage ([Rocha et al.](#)

2025). A larger sample will be required to confirm these conclusions.

6.6. OCN^- and Other Species in the $6.8\text{--}8.5 \mu\text{m}$ Region

Although our primary focus was the measurement of SO_2 and CH_4 ice abundances, our spectral fits included a total of ten ice species to accurately reproduce the blended absorption features observed between 6.8 and $8.5 \mu\text{m}$. Among these, the cyanate ion (OCN^-) plays an especially important role. As shown in Section 5.2, OCN^- is independently detected with NIRSpect, and its measured column densities are consistent with those derived from our MIRI fits in at least one source. This agreement strengthens confidence in its presence and highlights the value of near-infrared constraints for interpreting blended mid-infrared bands.

Consistent with [Rocha et al. \(2024\)](#), who demonstrated that the $7.68 \mu\text{m}$ absorption feature arises from a blend of SO_2 and OCN^- , we find that OCN^- contributes significantly in several of our sources. In Ser-emb 7 and L483, OCN^- appears across both pure and mixed SO_2 fits, while in IRAS 15398–3359 it is particularly important when adopting the $\text{CH}_3\text{OH}:\text{SO}_2$ mixture. The increased preference for OCN^- in cases where the SO_2 profile is broadened or weakened suggests that **Omnifit** may redistribute absorption strength between the two species.

Beyond OCN^- , ethanol ($\text{CH}_3\text{CH}_2\text{OH}$) and acetic acid (CH_3COOH) were also fit with relatively consistent appearances across several sources, though definitive detections remain uncertain. Ethanol was most consistently identified in IRAS 15398–3359 and L483, yielding average column densities of $8.3 \times 10^{17} \text{ cm}^{-2}$ and $9.8 \times 10^{17} \text{ cm}^{-2}$, respectively, with relative uncertainties of 42% and 45%. Acetic acid appeared across all four sources with typical column densities of $\sim 3 \times 10^{17} \text{ cm}^{-2}$. Both values are slightly higher than but broadly consistent with those reported by [Rocha et al. \(2024\)](#).

B335 yielded a significantly higher ethanol column density ($1.2 \times 10^{19} \text{ cm}^{-2}$), but the fit was associated with high uncertainty in continuum placement. Likewise, ethanol detection in Ser-emb 7 exhibited extreme sensitivity to baseline choice, with relative errors exceeding 400%. Given the relatively weak and blended nature of these features, and their strong dependence on baseline selection, we do not interpret these findings as definitive detections in this study. Rather, their inclusion was essential for achieving sound fits to the primary SO_2 and CH_4 absorptions, and they should be targeted for future dedicated analysis.

7. SUMMARY AND CONCLUSIONS

We have presented a new analysis of the 6.8–8.5 μm region in four Class 0 protostars (B335, L483, IRAS 15398–3359, and Ser-emb 7) from the CORINOS JWST MIRI MRS program. This region contains blended ice absorption features from CH_4 , SO_2 , and other organic species, and we focus on assessing the impact of baseline uncertainty on column density measurements of SO_2/CH_4 . Our conclusions are as follows:

- Measurements of CH_4 in all four targets show a clear CH_4 band at $\sim 7.7 \mu\text{m}$, with column densities on the order of $10^{17\text{--}18} \text{ cm}^{-2}$. These values imply that CH_4 is consistently detected in our sample and is consistent with previous ice fittings of low-mass protostars (e.g., Boogert et al. 2008).
- We show that SO_2 contributes to the blue shoulder of the $7.7 \mu\text{m}$ CH_4 band for IRAS 15398–3359, L483, and Ser-emb 7, with column densities on the order of $10^{16\text{--}17} \text{ cm}^{-2}$ using pure SO_2 and $\text{H}_2\text{O}:\text{SO}_2$ mixed laboratory ice data. For B335, however, the spectra are too noisy to confirm a detection, and any possible contribution from SO_2 should be regarded as tentative. This is consistent with (Rocha et al. 2024), who reported solid SO_2 detections in IRAS 2A but only tentative evidence in IRAS 23385, at similar column densities to our B335 limits. For the sources where SO_2 is detected (Ser-emb 7, L483, and IRAS 15398), the inferred SO_2/CH_4 ratios are 0.18–0.27, with lower values of ~ 0.04 in B335. When $\text{SO}_2:\text{CH}_3\text{OH}$ (1:1) mixtures are used instead, the SO_2/CH_4 ratios for all sources are reduced by a factor of several, to $\sim 0.01\text{--}0.04$. Fits with $\text{H}_2\text{O}:\text{SO}_2$ laboratory ice data yield intermediate ratios of 0.12–0.20, lying between the pure and CH_3OH mixed cases.
- OCN^- has a vibrational mode at $7.6 \mu\text{m}$ that coincides with the CH_4 and SO_2 features. This band was present in several of our fits, and the preference for OCN^- increased when the SO_2 profile was broadened or weakened, particularly for the pure or $\text{CH}_3\text{OH}:\text{SO}_2$ mixtures. By contrast, the $\text{H}_2\text{O}:\text{SO}_2$ mixture provided a better simultaneous fit to both SO_2 and OCN^- . In our sample, OCN^- was consistently detected in Ser-emb 7 and L483 across both pure and mixed SO_2 fits, and in IRAS 15398–3359 when using the $\text{CH}_3\text{OH}:\text{SO}_2$ mixture. Importantly, our independent JWST NIRSpec detection of the $4.6 \mu\text{m}$ OCN^- band in IRAS 15398–3359 yielded a column density broadly consistent with the value derived at $7.6 \mu\text{m}$ when using the $\text{H}_2\text{O}:\text{SO}_2$ mixture. This agreement strengthens confidence that both SO_2 and OCN^- contribute to the $7.6 \mu\text{m}$ absorption, and further supports the conclusion that $\text{H}_2\text{O}:\text{SO}_2$ mixtures provide the most realistic fits to the SO_2 feature.
- Our analysis demonstrates that the derived SO_2 column densities can vary based solely on the placement of the local continuum baseline. This baseline uncertainty typically dominates over the statistical fitting error from `Omnifit`, especially for pure SO_2 and $\text{H}_2\text{O}:\text{SO}_2$ fits. In contrast, the CH_4 column densities are relatively insensitive to baseline changes. Consequently, variations in the SO_2/CH_4 ratio are primarily driven by baseline placement. Nevertheless, across the four sources the ratios remain broadly similar within a factor of two, underscoring both the need for careful baseline treatment and the stability of the overall SO_2/CH_4 abundance relationship.
- We find no clear correlation between the SO_2/CH_4 ratio and luminosity, water-ice column density, envelope mass, or inclination. A slight decrease in SO_2/CH_4 with lower T_{bol} may be present, but the sample is too small to confirm this. These results suggest that other environmental factors not explored in this work, or initial chemical conditions, could play a key role in regulating sulfur ice chemistry.
- Finally, we emphasize the small sample of laboratory ice data available for SO_2 ices. Most existing analyses rely on just a few available profiles, such as $\text{SO}_2:\text{CH}_3\text{OH}$ (1:1), which may not reflect the full diversity of interstellar ice matrices. Additional mixtures are needed to reduce degeneracy in fitting and to more accurately interpret blended absorption features. More laboratory data made available from different temperatures and mixing ratios would significantly improve the ability to identify and quantify SO_2 ice contributions.

Our randomized baseline approach reveals how even small changes in continuum placement can alter the measured abundance of a weak feature in the 6.8–8.5 μm region within our four Class 0 sources. The results provide new constraints on the volatile sulfur budget and suggest that SO_2 ice could be responsible for a larger fraction of missing sulfur than previously predicted. However, the sensitivity of the SO_2 column density to baseline choice emphasizes the need for caution when interpreting these weak features, as well as the importance of statistical fitting methods.

8. ACKNOWLEDGMENTS

This work is based on observations made with the NASA/ ESA/CSA James Webb Space Telescope. The data were obtained from the Mikulski Archive for Space Telescopes at the Space Telescope Science Institute, which is operated by the Association of Universities for Research in Astronomy, Inc., under NASA contract NAS 5-03127 for JWST. These observations are associated with JWST GO Cycle 1 program ID 2151. The JWST data used in this paper can be found in MAST. R.E.G., L.I.C. and JDG acknowledge funding from JWST-GO-02151.001-A. R.E.G. acknowledges support from the UVA Interdisciplinary Doctoral Fellowship. Y.-L.Y. acknowledges support from Grant-in-Aid from the Ministry of Education, Culture, Sports, Science, and Tech-

nology of Japan (20H05844 and 25H00676). L.I.C. also acknowledges support from the Research Corporation for Science Advancement Cottrell Scholarship Award 28249, the David and Lucille Packard Foundation, and NSF AAG Award 2205698. R.T.G. thanks the National Science Foundation for funding through the Astronomy & Astrophysics program (grant number 2206516). R.E.G. thanks Dr. Suchitra Narayanan (Center for Astrophysics — Harvard & Smithsonian) for performing preliminary laboratory experiments that helped guide the direction of this work. We also thank the anonymous referee for constructive feedback that improved the clarity of this manuscript.

Facilities: JWST

Software: Omnipit (Suutarinen 2015)

REFERENCES

Agúndez, M., Marcelino, N., Cernicharo, J., Roueff, E., & Tafalla, M. 2019, *A&A*, 625, A147, doi: [10.1051/0004-6361/201935164](https://doi.org/10.1051/0004-6361/201935164)

Aikawa, Y., Wakelam, V., Garrod, R. T., & Herbst, E. 2008, *ApJ*, 674, 984, doi: [10.1086/524096](https://doi.org/10.1086/524096)

Altweegg, K., Combi, M., Fuselier, S. A., et al. 2022, *MNRAS*, 516, 3900, doi: [10.1093/mnras/stac2440](https://doi.org/10.1093/mnras/stac2440)

Anderson, D. E., Bergin, E. A., Maret, S., & Wakelam, V. 2013, *ApJ*, 779, 141, doi: [10.1088/0004-637X/779/2/141](https://doi.org/10.1088/0004-637X/779/2/141)

Andersson, S., Al-Halabi, A., Kroes, G. J., & van Dishoeck, E. F. 2006, *J. Chem. Phys.*, 124, 064715, doi: [10.1063/1.2162887](https://doi.org/10.1063/1.2162887)

Andersson, S., & van Dishoeck, E. F. 2008, *Astron. Astrophys.*, 491, 907, doi: [10.1051/0004-6361:200810071](https://doi.org/10.1051/0004-6361:200810071)

Artur de la Villarmois, E., Guzmán, V. V., Yang, Y.-L., Zhang, Y., & Sakai, N. 2023, *A&A*, 678, A124, doi: [10.1051/0004-6361/202346728](https://doi.org/10.1051/0004-6361/202346728)

Asplund, M., Grevesse, N., Sauval, A. J., & Scott, P. 2009, *Annual Review of Astronomy and Astrophysics*, 47, 481, doi: [10.1146/annurev-astro-082708-101642](https://doi.org/10.1146/annurev-astro-082708-101642)

Astropy Collaboration, Robitaille, T. P., Tollerud, E. J., et al. 2013, *A&A*, 558, A33, doi: [10.1051/0004-6361/201322068](https://doi.org/10.1051/0004-6361/201322068)

Astropy Collaboration, Price-Whelan, A. M., Sipócz, B. M., et al. 2018, *AJ*, 156, 123, doi: [10.3847/1538-3881/aabc4f](https://doi.org/10.3847/1538-3881/aabc4f)

Astropy Collaboration, Price-Whelan, A. M., Lim, P. L., et al. 2022, *ApJ*, 935, 167, doi: [10.3847/1538-4357/ac7c74](https://doi.org/10.3847/1538-4357/ac7c74)

Belloche, A., Garrod, R. T., Müller, H. S. P., et al. 2025, *Astronomy & Astrophysics*, 698, A143, doi: [10.1051/0004-6361/202554411](https://doi.org/10.1051/0004-6361/202554411)

Bergner, J. B., Martín-Doménech, R., Öberg, K. I., et al. 2019, *ACS Earth and Space Chemistry*, 3, 1564, doi: [10.1021/acsearthspacechem.9b00059](https://doi.org/10.1021/acsearthspacechem.9b00059)

Bisschop, S. E., Fuchs, G. W., Boogert, A. C. A., van Dishoeck, E. F., & Linnartz, H. 2007, *A&A*, 470, 749, doi: [10.1051/0004-6361:20077464](https://doi.org/10.1051/0004-6361:20077464)

Bjerkeli, P., Ramsey, J. P., Harsono, D., et al. 2019, *A&A*, 631, A64, doi: [10.1051/0004-6361/201935948](https://doi.org/10.1051/0004-6361/201935948)

Blake, G. A., Sutton, E. C., Masson, C. R., & Phillips, T. G. 1987, *The Astrophysical Journal*, 315, 621, doi: [10.1086/165023](https://doi.org/10.1086/165023)

Boogert, A. C. A., Brewer, K., Brittain, A., & Emerson, K. S. 2022, *ApJ*, 941, 32, doi: [10.3847/1538-4357/ac9b4a](https://doi.org/10.3847/1538-4357/ac9b4a)

Boogert, A. C. A., Gerakines, P. A., & Whittet, D. C. B. 2015, *ARA&A*, 53, 541, doi: [10.1146/annurev-astro-082214-122348](https://doi.org/10.1146/annurev-astro-082214-122348)

Boogert, A. C. A., Schutte, W. A., Helmich, F. P., Tielens, A. G. G. M., & Wooden, D. H. 1997, *A&A*, 317, 929

Boogert, A. C. A., Pontoppidan, K. M., Knez, C., et al. 2008, *ApJ*, 678, 985, doi: [10.1086/533425](https://doi.org/10.1086/533425)

Booth, A. S., van der Marel, N., Leemker, M., van Dishoeck, E. F., & Ohashi, S. 2021, *Astronomy & Astrophysics*, 648, doi: [10.1051/0004-6361/202038494](https://doi.org/10.1051/0004-6361/202038494)

Booth, A. S., Temmink, M., van Dishoeck, E. F., et al. 2024a, *Astronomical Journal*, 167, doi: [10.3847/1538-3881/ad03d1](https://doi.org/10.3847/1538-3881/ad03d1)

—. 2024b, *Astronomical Journal*, 167, doi: [10.3847/1538-3881/acdf01](https://doi.org/10.3847/1538-3881/acdf01)

Bradley, L., Sipócz, B., Robitaille, T., et al. 2023, *astropy/photutils*: 1.10.0, 1.10.0, Zenodo, doi: [10.5281/zenodo.1035865](https://doi.org/10.5281/zenodo.1035865)

Bulut, N., Roncero, O., Aguado, A., et al. 2021, *A&A*, 646, A5, doi: [10.1051/0004-6361/202039611](https://doi.org/10.1051/0004-6361/202039611)

Bushouse, H., Eisenhamer, J., Dencheva, N., et al. 2025, JWST Calibration Pipeline, 1.19.0, Zenodo, doi: [10.5281/zenodo.6984365](https://doi.org/10.5281/zenodo.6984365)

Chen, H., Myers, P. C., Ladd, E. F., & Wood, D. O. S. 1995, *ApJ*, 445, 377, doi: [10.1086/175703](https://doi.org/10.1086/175703)

Chen, Y., Rocha, W. R. M., van Dishoeck, E. F., et al. 2024, *A&A*, 690, A205, doi: [10.1051/0004-6361/202450706](https://doi.org/10.1051/0004-6361/202450706)

Chen, Y. J., Juang, K. J., Nuevo, M., et al. 2015, *ApJ*, 798, 80, doi: [10.1088/0004-637X/798/2/80](https://doi.org/10.1088/0004-637X/798/2/80)

Chu, L. E. U., Hodapp, K., & Boogert, A. 2020, *ApJ*, 904, 86, doi: [10.3847/1538-4357/abbfa5](https://doi.org/10.3847/1538-4357/abbfa5)

Cox, E. G., Novak, G., Sadavoy, S. I., et al. 2022, *ApJ*, 932, 34, doi: [10.3847/1538-4357/ac722a](https://doi.org/10.3847/1538-4357/ac722a)

Crapsi, A., van Dishoeck, E. F., Hogerheijde, M. R., Pontoppidan, K. M., & Dullemond, C. P. 2008, *A&A*, 486, 245, doi: [10.1051/0004-6361:20078589](https://doi.org/10.1051/0004-6361:20078589)

Dartois, E., Augé, B., Rothard, H., Boduch, P., & Brunetto, R. 2015, *Astronomy & Astrophysics*, 576, A125, doi: [10.1051/0004-6361/201425494](https://doi.org/10.1051/0004-6361/201425494)

Dartois, E., Demyk, K., d'Hendecourt, L., & Ehrenfreund, P. 1999a, *A&A*, 351, 1066

Dartois, E., Schutte, W., Geballe, T. R., et al. 1999b, *A&A*, 342, L32

Dartois, E., Thi, W. F., Geballe, T. R., et al. 2003, *A&A*, 399, 1009, doi: [10.1051/0004-6361:20021558](https://doi.org/10.1051/0004-6361:20021558)

Drozdovskaya, M. N., van Dishoeck, E. F., Jørgensen, J. K., et al. 2018, *MNRAS*, 476, 4949, doi: [10.1093/mnras/sty462](https://doi.org/10.1093/mnras/sty462)

Ehrenfreund, P., Boogert, A. C. A., Gerakines, P. A., et al. 1996, *A&A*, 315, L341

Ehrenfreund, P., Boogert, A. C. A., Gerakines, P. A., Tielens, A. G. G. M., & van Dishoeck, E. F. 1997, *A&A*, 328, 649

Enoch, M. L., Evans, II, N. J., Sargent, A. I., & Glenn, J. 2009, *ApJ*, 692, 973, doi: [10.1088/0004-637X/692/2/973](https://doi.org/10.1088/0004-637X/692/2/973)

Enoch, M. L., Corder, S., Duchêne, G., et al. 2011, *ApJS*, 195, 21, doi: [10.1088/0067-0049/195/2/21](https://doi.org/10.1088/0067-0049/195/2/21)

Esplugues, G., Fuente, A., Navarro-Almaida, D., et al. 2022, *A&A*, 662, A52, doi: [10.1051/0004-6361/202142936](https://doi.org/10.1051/0004-6361/202142936)

Evans, II, N. J., Di Francesco, J., Lee, J.-E., et al. 2015, *ApJ*, 814, 22, doi: [10.1088/0004-637X/814/1/22](https://doi.org/10.1088/0004-637X/814/1/22)

Evans, II, N. J., Yang, Y.-L., Green, J. D., et al. 2023, *ApJ*, 943, 90, doi: [10.3847/1538-4357/acaa38](https://doi.org/10.3847/1538-4357/acaa38)

Federman, S. A., Megeath, S. T., Rubinstein, A. E., et al. 2024, *ApJ*, 966, 41, doi: [10.3847/1538-4357/ad2fa0](https://doi.org/10.3847/1538-4357/ad2fa0)

Ferrari, P., Berden, G., Redlich, B., Waters, L. B. F. M., & Bakker, J. M. 2024, *Nature Communications*, 15, 5928, doi: [10.1038/s41467-024-50303-2](https://doi.org/10.1038/s41467-024-50303-2)

Foreman-Mackey, D., Hogg, D. W., Lang, D., & Goodman, J. 2013, *PASP*, 125, 306, doi: [10.1086/670067](https://doi.org/10.1086/670067)

Francis, L., van Gelder, M. L., van Dishoeck, E. F., et al. 2024, *A&A*, 683, A249, doi: [10.1051/0004-6361/202348105](https://doi.org/10.1051/0004-6361/202348105)

Fuente, A., Cernicharo, J., Agúndez, M., et al. 2010, *A&A*, 524, A19, doi: [10.1051/0004-6361/201014905](https://doi.org/10.1051/0004-6361/201014905)

Galli, P. A. B., Bouy, H., Olivares, J., et al. 2020, *A&A*, 643, A148, doi: [10.1051/0004-6361/202038717](https://doi.org/10.1051/0004-6361/202038717)

Gálvez, O., Maté, B., Herrero, V. J., & Escribano, R. 2010, *ApJ*, 724, 539, doi: [10.1088/0004-637X/724/1/539](https://doi.org/10.1088/0004-637X/724/1/539)

Garozzo, M., Fulvio, D., Kanuchova, Z., Palumbo, M. E., & Strazzulla, G. 2010, *A&A*, 509, A67, doi: [10.1051/0004-6361/200913040](https://doi.org/10.1051/0004-6361/200913040)

Gerakines, P. A., Schutte, W. A., & Ehrenfreund, P. 1996, *A&A*, 312, 289

Gerakines, P. A., Schutte, W. A., Greenberg, J. M., & van Dishoeck, E. F. 1995, *A&A*, 296, 810, doi: [10.48550/arXiv.astro-ph/9409076](https://doi.org/10.48550/arXiv.astro-ph/9409076)

Gibb, E. L., Whittet, D. C. B., Boogert, A. C. A., & Tielens, A. G. G. M. 2004, *ApJS*, 151, 35, doi: [10.1086/381182](https://doi.org/10.1086/381182)

Grim, R. J. A., Baas, F., Geballe, T. R., Greenberg, J. M., & Schutte, W. A. 1991, *A&A*, 243, 473

Gudipati, M. S., Brunetto, R., Dartois, E., & Strazzulla, G. 2023, *Annual Review of Astronomy and Astrophysics*, 61, 245, doi: [10.1146/annurev-astro-032620-115543](https://doi.org/10.1146/annurev-astro-032620-115543)

Hama, T., & Watanabe, N. 2013, *Chemical Reviews*, 113, 8783, doi: [10.1021/cr4000978](https://doi.org/10.1021/cr4000978)

Harvey, D. W. A., Wilner, D. J., Lada, C. J., et al. 2001, *ApJ*, 563, 903, doi: [10.1086/324076](https://doi.org/10.1086/324076)

Herbst, E., & van Dishoeck, E. F. 2009, *ARA&A*, 47, 427, doi: [10.1146/annurev-astro-082708-101654](https://doi.org/10.1146/annurev-astro-082708-101654)

Heyer, M. H., & Graham, J. A. 1989, *PASP*, 101, 816, doi: [10.1086/132502](https://doi.org/10.1086/132502)

Hirota, T., Lefloch, B., Oya, Y., et al. 2025, *A&A*, 695, A278, doi: [10.1051/0004-6361/202453386](https://doi.org/10.1051/0004-6361/202453386)

Huang, T. S., Yang, G. H., & Tang, G. Y. 1979, *IEEE Transactions on Acoustics, Speech, and Signal Processing*, 27, 13

Imai, M., Sakai, N., Oya, Y., et al. 2016, *ApJL*, 830, L37, doi: [10.3847/2041-8205/830/2/L37](https://doi.org/10.3847/2041-8205/830/2/L37)

Ivlev, A. V., Padovani, M., Galli, D., & Caselli, P. 2015, *The Astrophysical Journal*, 812, 135, doi: [10.1088/0004-637X/812/2/135](https://doi.org/10.1088/0004-637X/812/2/135)

Jacobsen, S. K., Jørgensen, J. K., Di Francesco, J., et al. 2019, *A&A*, 629, A29, doi: [10.1051/0004-6361/201833214](https://doi.org/10.1051/0004-6361/201833214)

Jørgensen, J. K., Belloche, A., & Garrod, R. T. 2020, *ARA&A*, 58, 727, doi: [10.1146/annurev-astro-032620-021927](https://doi.org/10.1146/annurev-astro-032620-021927)

Jørgensen, J. K., Schöier, F. L., & van Dishoeck, E. F. 2002, *A&A*, 389, 908, doi: [10.1051/0004-6361:20020681](https://doi.org/10.1051/0004-6361:20020681)

—. 2004, *A&A*, 416, 603, doi: [10.1051/0004-6361:20034440](https://doi.org/10.1051/0004-6361:20034440)

Jørgensen, J. K., Visser, R., Sakai, N., et al. 2013, *ApJL*, 779, L22, doi: [10.1088/2041-8205/779/2/L22](https://doi.org/10.1088/2041-8205/779/2/L22)

Jørgensen, J. K., van der Wiel, M. H. D., Coutens, A., et al. 2016, *A&A*, 595, A117, doi: [10.1051/0004-6361/201628648](https://doi.org/10.1051/0004-6361/201628648)

Kerkhof, O., Schutte, W. A., & Ehrenfreund, P. 1999, *A&A*, 346, 990

Laas, J. C., & Caselli, P. 2019, *A&A*, 624, A108, doi: [10.1051/0004-6361/201834446](https://doi.org/10.1051/0004-6361/201834446)

Lee, J.-E., Evans, N. J., Baek, G., et al. 2025, *ApJL*, 978, L3, doi: [10.3847/2041-8213/ad841f](https://doi.org/10.3847/2041-8213/ad841f)

Lee, S., Lee, J.-E., & Bergin, E. A. 2015, *ApJS*, 217, 30, doi: [10.1088/0067-0049/217/2/30](https://doi.org/10.1088/0067-0049/217/2/30)

McClure, M. K., Pontoppidan, K. M., Rocha, W. R. M., & the ICE AGE team. 2023, *The Astrophysical Journal Letters*, 945, L23, doi: [10.3847/2041-8213/acb4d8](https://doi.org/10.3847/2041-8213/acb4d8)

Myers, P. C., & Ladd, E. F. 1993, *ApJL*, 413, L47, doi: [10.1086/186956](https://doi.org/10.1086/186956)

Navarro-Almaida, D., Le Gal, R., Fuente, A., et al. 2020, *A&A*, 637, A39, doi: [10.1051/0004-6361/201937180](https://doi.org/10.1051/0004-6361/201937180)

Nazari, P., Rocha, W. R. M., Rubinstein, A. E., et al. 2024, *A&A*, 686, A71, doi: [10.1051/0004-6361/202348695](https://doi.org/10.1051/0004-6361/202348695)

Novozamsky, J. H., Schutte, W. A., Keane, J. V., & Tielens, A. G. G. M. 2001, *Astronomy & Astrophysics*, 379, 588, doi: [10.1051/0004-6361:20011309](https://doi.org/10.1051/0004-6361:20011309)

Oba, Y., Watanabe, N., Hama, T., et al. 2018, *Monthly Notices of the Royal Astronomical Society*, 475, 2311, doi: [10.1093/mnras/stx3315](https://doi.org/10.1093/mnras/stx3315)

Öberg, K. I., Boogert, A. C. A., Pontoppidan, K. M., et al. 2008, *ApJ*, 678, 1032, doi: [10.1086/533432](https://doi.org/10.1086/533432)

—. 2011a, *ApJ*, 740, 109, doi: [10.1088/0004-637X/740/2/109](https://doi.org/10.1088/0004-637X/740/2/109)

—. 2011b, *ApJ*, 740, 109, doi: [10.1088/0004-637X/740/2/109](https://doi.org/10.1088/0004-637X/740/2/109)

Öberg, K. I., Fraser, H. J., Boogert, A. C. A., et al. 2007, *A&A*, 462, 1187, doi: [10.1051/0004-6361:20065881](https://doi.org/10.1051/0004-6361:20065881)

Ohashi, N., Tobin, J. J., Jørgensen, J. K., et al. 2023, *ApJ*, 951, 8, doi: [10.3847/1538-4357/acd384](https://doi.org/10.3847/1538-4357/acd384)

Okoda, Y., Oya, Y., Imai, M., et al. 2022, *ApJ*, 935, 136, doi: [10.3847/1538-4357/ac7ff4](https://doi.org/10.3847/1538-4357/ac7ff4)

Okoda, Y., Oya, Y., Sakai, N., et al. 2024, *ApJ*, 970, 28, doi: [10.3847/1538-4357/ad4d88](https://doi.org/10.3847/1538-4357/ad4d88)

Okoda, Y., Oya, Y., Francis, L., et al. 2021, *ApJ*, 910, 11, doi: [10.3847/1538-4357/abddb1](https://doi.org/10.3847/1538-4357/abddb1)

Ortiz-León, G. N., Dzib, S. A., Kounkel, M. A., et al. 2017, *ApJ*, 834, 143, doi: [10.3847/1538-4357/834/2/143](https://doi.org/10.3847/1538-4357/834/2/143)

Palumbo, M. E., Tielens, A. G. G. M., & Tokunaga, A. T. 1995, *The Astrophysical Journal*, 449, 674, doi: [10.1086/176061](https://doi.org/10.1086/176061)

Perotti, G., Jørgensen, J. K., Fraser, H. J., et al. 2021, *A&A*, 650, A168, doi: [10.1051/0004-6361/202039669](https://doi.org/10.1051/0004-6361/202039669)

Pontoppidan, K. M., Dullemond, C. P., van Dishoeck, E. F., et al. 2005, *ApJ*, 622, 463, doi: [10.1086/427688](https://doi.org/10.1086/427688)

Pontoppidan, K. M., van Dishoeck, E. F., & Dartois, E. 2004, *A&A*, 426, 925, doi: [10.1051/0004-6361:20041276](https://doi.org/10.1051/0004-6361:20041276)

Pontoppidan, K. M., Fraser, H. J., Dartois, E., et al. 2003, *Astronomy & Astrophysics*, 408, 981, doi: [10.1051/0004-6361:20031071](https://doi.org/10.1051/0004-6361:20031071)

Qasim, D., Chuang, K. J., Fedoseev, G., et al. 2018, *A&A*, 612, A83, doi: [10.1051/0004-6361/201732355](https://doi.org/10.1051/0004-6361/201732355)

Rachid, M. G., Terwisscha van Scheltinga, J., Koletzki, D., et al. 2020, in *IAU Symposium*, Vol. 350, *Laboratory Astrophysics: From Observations to Interpretation*, ed. F. Salama & H. Linnartz, 420–421, doi: [10.1017/S1743921319009827](https://doi.org/10.1017/S1743921319009827)

Rayalacheruvu, P., Majumdar, L., Rocha, W. R. M., et al. 2025, arXiv e-prints. <https://arxiv.org/abs/2506.15358>

Rieke, G. H., Ressler, M. E., Morrison, J. E., et al. 2015, *PASP*, 127, 665, doi: [10.1086/682257](https://doi.org/10.1086/682257)

Rocha, W. R. M., Perotti, G., Kristensen, L. E., & Jørgensen, J. K. 2021, *A&A*, 654, A158, doi: [10.1051/0004-6361/202039360](https://doi.org/10.1051/0004-6361/202039360)

Rocha, W. R. M., Rachid, M. G., Olsthoorn, B., et al. 2022, *A&A*, 668, A63, doi: [10.1051/0004-6361/202244032](https://doi.org/10.1051/0004-6361/202244032)

Rocha, W. R. M., van Dishoeck, E. F., Ressler, M. E., et al. 2024, *A&A*, 683, A124, doi: [10.1051/0004-6361/202348427](https://doi.org/10.1051/0004-6361/202348427)

Rocha, W. R. M., McClure, M. K., Sturm, J. A., et al. 2025, *A&A*, 693, A288, doi: [10.1051/0004-6361/202451505](https://doi.org/10.1051/0004-6361/202451505)

Saito, M., Sunada, K., Kawabe, R., Kitamura, Y., & Hirano, N. 1999, *ApJ*, 518, 334, doi: [10.1086/307244](https://doi.org/10.1086/307244)

Sakai, N., Sakai, T., Hirota, T., Burton, M., & Yamamoto, S. 2009, *ApJ*, 697, 769, doi: [10.1088/0004-637X/697/1/769](https://doi.org/10.1088/0004-637X/697/1/769)

Sakai, N., Sakai, T., Hirota, T., & Yamamoto, S. 2008, *ApJ*, 672, 371, doi: [10.1086/523635](https://doi.org/10.1086/523635)

San José-García, I., Mottram, J. C., Kristensen, L. E., et al. 2013, *A&A*, 553, A125, doi: [10.1051/0004-6361/201220472](https://doi.org/10.1051/0004-6361/201220472)

Santos, J. C., Linnartz, H., & Chuang, K. J. 2024, *A&A*, 690, A24, doi: [10.1051/0004-6361/202451368](https://doi.org/10.1051/0004-6361/202451368)

Savitzky, A., & Golay, M. J. E. 1964, *Analytical Chemistry*, 36, 1627, doi: [10.1021/ac60214a047](https://doi.org/10.1021/ac60214a047)

Schutte, W. A., Boogert, A. C. A., Tielens, A. G. G. M., et al. 1999, *A&A*, 343, 966

Semenov, D., Favre, C., Fedele, D., et al. 2018, *A&A*, 617, A28, doi: [10.1051/0004-6361/201832980](https://doi.org/10.1051/0004-6361/201832980)

Shimonishi, T., Onaka, T., Kato, D., et al. 2010, *A&A*, 514, A12, doi: [10.1051/0004-6361/200913815](https://doi.org/10.1051/0004-6361/200913815)

Shingledecker, C. N., & Herbst, E. 2018, *Physical Chemistry Chemical Physics*, 20, 5359, doi: [10.1039/C7CP07919C](https://doi.org/10.1039/C7CP07919C)

Shingledecker, C. N., Lamberts, T., Laas, J. C., et al. 2020, *ApJ*, 888, 52, doi: [10.3847/1538-4357/ab5360](https://doi.org/10.3847/1538-4357/ab5360)

Slavicinska, K., Boogert, A. C. A., Tychoniec, L., et al. 2025, *A&A*, 693, A146, doi: [10.1051/0004-6361/202451383](https://doi.org/10.1051/0004-6361/202451383)

Smith, A. M., Stecher, T. P., & Casswell, L. 1980, *ApJ*, 242, 402, doi: [10.1086/158473](https://doi.org/10.1086/158473)

Suutarinen, A. 2015, Phd thesis, The Open University. <http://oro.open.ac.uk/61309/>

Suutarinen, A. 2015, omnifit: v0.2.1, v0.2.1, Zenodo, doi: [10.5281/zenodo.35536](https://doi.org/10.5281/zenodo.35536)

Tafalla, M., Myers, P. C., Mardones, D., & Bachiller, R. 2000, *A&A*, 359, 967, doi: [10.48550/arXiv.astro-ph/0005525](https://doi.org/10.48550/arXiv.astro-ph/0005525)

Taillard, A., Martín-Doménech, R., Carrascosa, H., et al. 2025, *A&A*, 694, A263, doi: [10.1051/0004-6361/202452900](https://doi.org/10.1051/0004-6361/202452900)

Terwisscha van Scheltinga, J., Ligterink, N. F. W., Boogert, A. C. A., van Dishoeck, E. F., & Linmartz, H. 2018, *A&A*, 611, A35, doi: [10.1051/0004-6361/201731998](https://doi.org/10.1051/0004-6361/201731998)

Terwisscha van Scheltinga, J., Hogerheijde, M. R., Cleeves, L. I., et al. 2021, *ApJ*, 906, 111, doi: [10.3847/1538-4357/abc9ba](https://doi.org/10.3847/1538-4357/abc9ba)

Thieme, T. J., Lai, S.-P., Ohashi, N., et al. 2023, *ApJ*, 958, 60, doi: [10.3847/1538-4357/ad003a](https://doi.org/10.3847/1538-4357/ad003a)

Tieftrunk, A., Pineau des Forets, G., Schilke, P., & Walmsley, C. M. 1994, *A&A*, 289, 579

Tobin, J. J., Hartmann, L., Calvet, N., & D'Alessio, P. 2008, *ApJ*, 679, 1364, doi: [10.1086/587683](https://doi.org/10.1086/587683)

van Broekhuizen, F. A., Pontoppidan, K. M., Fraser, H. J., & van Dishoeck, E. F. 2005, *A&A*, 441, 249, doi: [10.1051/0004-6361:20041711](https://doi.org/10.1051/0004-6361:20041711)

van Dishoeck, E. F., & Bergin, E. A. 2021, in *ExoFrontiers; Big Questions in Exoplanetary Science*, ed. N. Madhusudhan, 14–1, doi: [10.1088/2514-3433/abfa8fch14](https://doi.org/10.1088/2514-3433/abfa8fch14)

van Dishoeck, E. F., Kristensen, L. E., Mottram, J. C., et al. 2021, *A&A*, 648, A24, doi: [10.1051/0004-6361/202039084](https://doi.org/10.1051/0004-6361/202039084)

van Dishoeck, E. F., Tychoniec, L., Rocha, W. R. M., et al. 2025, arXiv e-prints, arXiv:2505.08002, doi: [10.48550/arXiv.2505.08002](https://doi.org/10.48550/arXiv.2505.08002)

Vastel, C., Quénard, D., Le Gal, R., et al. 2018, *MNRAS*, 478, 5514, doi: [10.1093/mnras/sty1336](https://doi.org/10.1093/mnras/sty1336)

Virtanen, P., Gommers, R., Oliphant, T. E., et al. 2020, *Nature Methods*, 17, 261, doi: [10.1038/s41592-019-0686-2](https://doi.org/10.1038/s41592-019-0686-2)

Wakelam, V., Caselli, P., Ceccarelli, C., Herbst, E., & Castets, A. 2004, *A&A*, 422, 159, doi: [10.1051/0004-6361:20047186](https://doi.org/10.1051/0004-6361:20047186)

Wells, M., Pel, J. W., Glassee, A., et al. 2015, *PASP*, 127, 646, doi: [10.1086/682281](https://doi.org/10.1086/682281)

Woods, P. M., Occhiogrosso, A., Viti, S., et al. 2015, *Monthly Notices of the Royal Astronomical Society*, 450, 1256, doi: [10.1093/mnras/stv652](https://doi.org/10.1093/mnras/stv652)

Wright, G. S., Wright, D., Goodson, G. B., et al. 2015, *PASP*, 127, 595, doi: [10.1086/682253](https://doi.org/10.1086/682253)

Yang, Y.-L., Green, J. D., Pontoppidan, K. M., et al. 2022, *ApJL*, 941, L13, doi: [10.3847/2041-8213/aca289](https://doi.org/10.3847/2041-8213/aca289)

Yarnall, Y. Y., & Hudson, R. L. 2022, *ApJL*, 931, L4, doi: [10.3847/2041-8213/ac6b32](https://doi.org/10.3847/2041-8213/ac6b32)

Yen, H.-W., Takakuwa, S., Koch, P. M., et al. 2015, *ApJ*, 812, 129, doi: [10.1088/0004-637X/812/2/129](https://doi.org/10.1088/0004-637X/812/2/129)

Zhou, S., Evans, II, N. J., Koempe, C., & Walmsley, C. M. 1993, *ApJ*, 404, 232, doi: [10.1086/172271](https://doi.org/10.1086/172271)

Öberg, K. I., Bottinelli, S., & van Dishoeck, E. F. 2009, *Astronomy & Astrophysics*, 494, L13, doi: [10.1051/0004-6361:200811471](https://doi.org/10.1051/0004-6361:200811471)

APPENDIX

A. SO₂ LABORATORY DATA

The differences between the pure SO₂, H₂O:SO₂ (10:1), and SO₂:CH₃OH(1:1) laboratory spectra are due to the mixed matrix altering the vibrational mode for the pure species. In the mixture, CH₃OH causes broadening and weakening of the 7.6 μm absorption feature. Despite unknown thickness in the mixed CH₃OH ice experiment, the use of `Omnifit` compensates for such differences by scaling the laboratory profiles during fitting. The reduced contribution of the mixed SO₂ spectrum in the `Omnifit` results is not due to the absolute strength of the feature seen in the lab data of Fig. 13, but because the broader, shallower profile does not match as well to the observed absorption feature compared to the pure SO₂ profile Boogert et al. (1997), or the H₂O:SO₂ profile Yarnall & Hudson (2022). The pure and CH₃OH mixed ices are the only available SO₂ ice data on the LIDA database to download and use in the fittings of this feature, which stresses the necessity of obtaining more laboratory data for SO₂. The H₂O:SO₂ spectra is taken from Yarnall & Hudson (2022), and the feature is blue-shifted compared to the CH₃OH mixture.

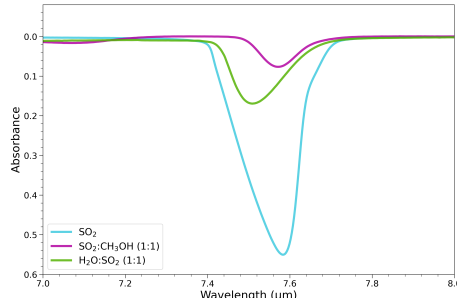


Figure 13. SO₂ laboratory data for pure and CH₃OH mixed ices taken from Boogert et al. (1997) and the Goddard Ice Database. Note how the peak of SO₂ changes depending on mixture and temperature. Only the low temperature pure and mixed ice were used in this study for comparison.

B. H₂O ICE MEASUREMENTS

Water ice is the most abundant species in ice mantle. While our MIRI MRS spectra do not cover the strongest H₂O stretching mode at $\sim 3 \mu\text{m}$, we can use the H₂O libration mode at $\sim 13.6 \mu\text{m}$ to measure the H₂O ice column density. The broad libration mode mostly blends with the silicate dust absorption at $\sim 10 \mu\text{m}$. To model this H₂O band, we use the silicate-subtracted optical depth spectra presented in Turner et al. (in prep.).

We describe a brief outline of the steps leading to these spectra, while refer the details to their study. The silicate dust absorption is fitted with two compositions, pyroxene and forsterite, simultaneously with a polynomial baseline. The anchor points are chosen at ~ 5 , ~ 8 and $\gtrsim 20 \mu\text{m}$. Figure 14 shows the silicate-subtracted optical depth spectra of the CORINOS sources. The spectrum of L483 is further smoothed with a median filter using a kernel size of 31 to remove the impact of emission lines. Moreover, we removed residual offset in the optical spectrum of L483 with a simple straight baseline (Figure 14).

Figure 14 shows clear absorption feature at 10-18 μm , consistent with the H₂O ice libration mode. We started the modeling with only a low-temperature H₂O ice component (e.g., 15 K); however, the broad absorption feature at 10-18 μm cannot be reproduced with a single component. We employed a low- and high-temperature H₂O component, 15 K and 135 K, to fit the feature. The H₂O ice laboratory spectra are taken from Öberg et al. (2007), processed with a local baseline subtraction fitted with a second-order polynomial to isolate the libration mode. We optimized the contributions from these two H₂O ice components using the Trust Region Reflective algorithm and least squares minimization implemented in `astropy` (Astropy Collaboration et al. 2013, 2018, 2022). Figure 14 shows the best-fitting H₂O ice spectra and Table 5 lists the fitted H₂O column densities.

Table 5. Fitted H₂O column densities

Source	15 K	135 K	Total (10^{19} cm^{-2})
B335	4.80	...	4.80
IRAS 15398–3359	0.27	1.51	1.78
L483	1.43	0.93	2.36
Ser-emb 7	1.11	...	1.11

Note: The high-temperature H₂O ice component is not detected in B335 and Ser-emb 7.

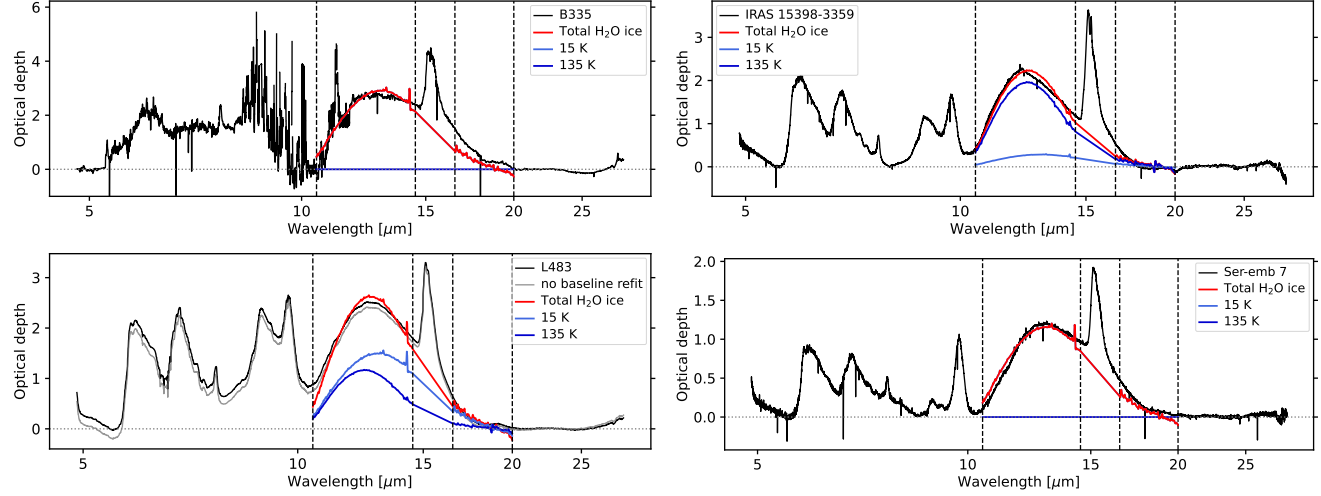


Figure 14. Best-fitting H₂O ice spectra in the CORINOS sources, shown in red. The black line shows the silicate-subtracted optical depth spectra, while the fitted 15 K and 135 K H₂O ice components are shown in light blue and dark blue lines, respectively. The light gray line in the L483 spectrum is the optical depth spectra without additional baseline calibration (see text). The vertical dashed lines indicate the wavelength ranges, 10.5–14.5 μm and 16.5–20 μm , where the H₂O ice spectra are optimized.